JGR Solid Earth

RESEARCH ARTICLE
10.1029/2018JB016670

Key Points:

- Seismicity induced by Groningen gas depletion can be modelled by a Coulomb rate-and-state approach
- Characteristic periods of stress perturbations are much shorter than the inferred intrinsic time delay of the earthquake-nucleation process
- The Groningen fault system in the two sub-areas of interest is gradually becoming more sensitive to the stressing rate

Supporting Information:

- Supporting Information S1

Correspondence to:
T. Candela,
thibault.g.candela@gmail.com

Citation:
Candela, T., Osinga, S., Ampuero, J.-P., Wassing, B., Pluymaekers, M., Fokker, P. A., et al. (2019). Depletion-induced seismicity at the Groningen gas field: Coulomb rate-and-state models including differential compaction effect. *Journal of Geophysical Research: Solid Earth*, *124*. https://doi.org/10.1029/2018JB016670

Received 7 SEP 2018
Accepted 20 JUN 2019
Accepted article online 30 JUN 2019

Depletion-Induced Seismicity at the Groningen Gas Field: Coulomb Rate-and-State Models Including Differential Compaction Effect

Thibault Candela[1], Sander Osinga[1], Jean-Paul Ampuero[2], Brecht Wassing[1], Maarten Pluymaekers[1], Peter A. Fokker[1,3], Jan-Diederik van Wees[1,3], Hans A. de Waal[4], and Annemarie G. Muntendam-Bos[4]

[1]TNO, Geological Survey of the Netherlands, Utrecht, The Netherlands, [2]Université Côte d'Azur, IRD, CNRS, Observatoire de la Côte d'Azur, Géoazur, Sophia Antipolis, France, [3]Department of Geosciences, Utrecht University, Utrecht, The Netherlands, [4]State Supervision of Mines, The Hague, The Netherlands

Abstract We implement a Coulomb rate-and-state approach to explore the nonlinear relation between stressing rate and seismicity rate in the Groningen gas field. Coulomb stress rates are calculated, taking into account the 3-D structural complexity of the field and including the poroelastic effect of the differential compaction due to fault offsets. The spatiotemporal evolution of the Groningen seismicity must be attributed to a combination of both (i) spatial variability in the induced stressing rate history and (ii) spatial heterogeneities in the rate-and-state model parameters. Focusing on two subareas of the Groningen field where the observed event rates are very contrasted even though the modeled seismicity rates are of similar magnitudes, we show that the rate-and-state model parameters are spatially heterogeneous. For these two subareas, the very low background seismicity rate of the Groningen gas field can explain the long delay in the seismicity response relative to the onset of reservoir depletion. The characteristic periods of stress perturbations, due to gas production fluctuations, are much shorter than the inferred intrinsic time delay of the earthquake nucleation process. In this regime the modeled seismicity rate is in phase with the stress changes. However, since the start of production and for two subareas of our analysis, the Groningen fault system is unsteady and it is gradually becoming more sensitive to the stressing rate.

1. Introduction

The seismicity at the Groningen field, in The Netherlands, has triggered several studies aiming at improving our knowledge about seismicity induced by reservoir depletion (see Candela et al., 2018; Van Geuns & Thienen-Visser, 2017, for a review). The recent, relatively large induced earthquake (M 3.4) in January 2018 was another alarm urging to build comprehensive seismological models capable of explaining the spatiotemporal distribution of the recorded seismicity. The present manuscript proposes such a model.

The goal of our seismological model is to translate pressure depletion of the Groningen gas field into seismicity. At least three other seismological models have been published so far for that goal. Bourne et al. (2014) proposed a strain-based model directly connecting reservoir compaction at faults to seismicity. This approach was later coupled by Bourne and Oates (2017) and Bourne et al. (2018) with an analytical approximation of the Coulomb stresses induced by reservoir depletion. Dempsey and Suckale (2017) proposed an approach coupling Coulomb failure and fracture mechanics theory to derive induced seismicity. In these three attempts, detailed spatiotemporal pressure fields from reservoir simulations were used as input. However, approximations were made to model the poroelastic contribution to stress changes induced by the reservoir compaction on the multiple faults that crisscross the reservoir. We propose here a semianalytical approach honoring this poroelastic contribution in the context of the highly faulted Groningen field. More specifically, the effect of differential compaction between reservoir compartments that are offset by faults, considered of prime importance for stress buildup in compacting reservoirs (Buijze et al., 2017; Mulders, 2003; Orlic & Wassing, 2013; Roest & Kuilman, 1994; Van den Bogert, 2015; van Wees et al., 2014), is explicitly modeled in our approach.

Instead of modeling the entire Groningen field as has been done in the previous attempts (Bourne et al., 2014; Bourne et al., 2018; Bourne & Oates, 2017; Dempsey & Suckale, 2017), we chose to focus our study

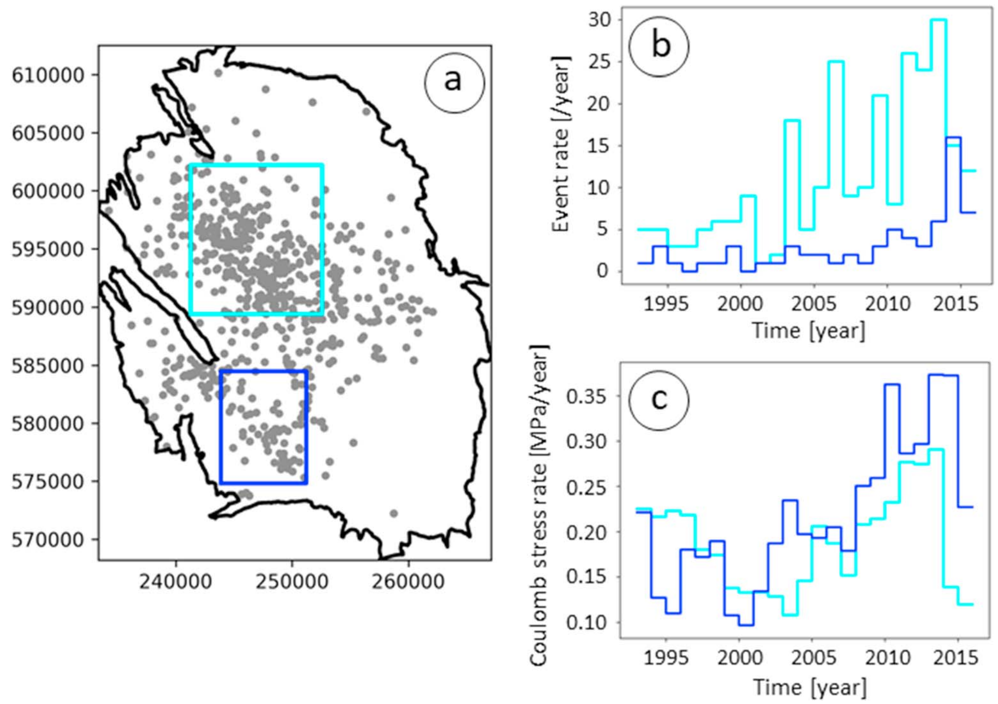

Figure 1. Contrasted seismicity and stress history of the two subareas of interest in the Groningen gas field. (a) Location of the two selected subareas (cyan: C-area, blue: SW-area) inside the Groningen gas field (black contour). (b) Observed yearly event rates with a minimum magnitude of 1.0. (c) Modeled yearly Coulomb stress rates for the two subareas.

on two subareas: (i) the central area where the seismicity rates are the highest and (ii) the southwest area which has a much lower seismic activity (Figure 1). In previous models considering the entire Groningen field, the resolution was limited since the parameters of the seismological model were assumed to be spatially homogeneous. Our approach offers the opportunity to link differences in the seismicity evolution between the two subareas of the field with differences in seismological model parameters.

From the onset of production in the Groningen gas field in 1968 up to the oil crisis in 1976 the average depletion rate was relatively high. From 1976 to 2000 the average production rate of the field was progressively decreased. After 2000, in order to match the increasing market demand, the production rate was reincreased. At the same time of this reincreased of the production rate, the seismicity rate significantly increased (Muntendam-Bos & de Waal, 2013). By the end of 2013 the seismicity rate had increased significantly and in January 2014, a reduction of gas production was imposed by the Dutch government. These changes in production rates over time call for an approach exploring the relationship between stressing rate and seismicity rate (Figures 1b and 1c). We propose to couple our calculation of Coulomb stress induced by reservoir depletion on faults with the constitutive law for the evolution of seismicity derived by Dieterich (1994). Dieterich's theory links seismicity rates with stress perturbations and is based on an empirical fault friction law derived from a body of laboratory experiments carried at sliding speeds representative of earthquake nucleation. This theory has been applied in a variety of contexts to model the response of seismicity to seismic stress perturbations, such as aftershock sequences triggered by the coseismic stress changes of a mainshock (e.g., Cattania et al., 2015; Hainzl et al., 2009) and aseismic stress perturbations due to volcanic activity (Dieterich et al., 2000; Llenos et al., 2009; Toda et al., 2002), slow slip transients (Inbal et al., 2017), tides (Ader et al., 2014), and injection-induced seismicity (Segall & Lu, 2015). Chang and Segall (2016a, 2016b) have recently used Dieterich's theory for seismicity on basement faults induced by fluid extraction of the overburden reservoir. Here, along the same lines, Dieterich's theory is applied and tested in the context of depletion-induced seismicity within the reservoir. More specifically, we propose to establish the validity of Dieterich's approach using observations of induced seismicity at Groningen gas field.

Two independent Bayesian approaches, Brute-Force grid search and MCMC (Markov Chain Monte Carlo; Foreman-Mackey et al., 2013), have been considered here to explore the prior space of each of the model parameters of Dieterich's theory and to constrain them, incorporating in both cases the earthquake observations with a nonhomogeneous Poisson process. Both approaches showed coherent results and confirmed that the data are sufficiently informational to constrain the model parameters. In particular, our results show that Dieterich's theory can explain and can give a physical basis to the nonlinear increase of seismicity rates observed at the Groningen gas field.

2. Methodology

2.1. From Reservoir Depletion to Stress Rate at Faults

The pore pressure evolution of the entire Groningen gas field and surrounding aquifers is computed, by the field operators, via a two-component (gas and water) reservoir flow simulator honoring heterogeneous hydraulic/mechanical parameters. The reader is referred to NAM (2016, 2017) for the details about the model parameters, model geometry, layering, faults, and history matching procedure. Of particular interest here, the rock compressibility was inferred from inversion of subsidence data. The 3-D numerical flow model for the full field contains approximately 650,000 cells, with an average cell size of 725 × 725 m and cell thickness of 5–10 m. The simulated pressure fields are the result of the match of the historical production from all wells in the field based on mass rate constraint. The two selected subareas (Figure 1a) for the present study are two cutouts of that single full field model.

The average pressure drop over the Groningen field since the start of production is approximately 22 MPa. The direct effect of this pore pressure drop involves an increase of the effective normal stress on the faults and thus a direct clamping of the faults tending to stabilize them. The fault destabilization is due to the poroelastic stress changes induced by the reservoir compaction (Segall & Fitzgerald, 1998). The reduction of the pore pressure leads to reservoir contraction and a reduction of the horizontal stress, which partially counteracts the increased clamping caused by the direct pore pressure effect. The vertical stress remains unaffected by the rock contraction, which means that the shear stresses along the nearly vertical faults of the Groningen field increase with ongoing pore pressure depletion and might reach failure.

However, this picture of the stress evolution during reservoir depletion is valid only if we consider an elastic homogeneous thin reservoir (Segall & Fitzgerald, 1998). Differential compaction between two juxtaposed reservoir compartments vertically offset by a fault has been shown to be a dominant factor in the induced stress buildup along faults during reservoir depletion (Buijze et al., 2017; Mulders, 2003; Orlic & Wassing, 2013; Roest & Kuilman, 1994; Van den Bogert, 2015; van Wees et al., 2014; van Wees et al., 2017). If we consider faults with offsets, it is rather complicated to derive an analytical expression for the depletion-induced stress changes. We have therefore implemented a seminumerical approach (MACRIS, Mechanical Analysis of Complex Reservoirs for Induced Seismicity) to specifically handle this effect of fault offset.

The main specificity of MACRIS is that it is a mesh-free approach where there is no need to build a dedicated grid for the geomechanical analysis. MACRIS takes directly as input the grid of the reservoir flow simulation, in our case the 3-D pressure fields of the Groningen gas field at a yearly sampling rate. Each grid block of the reservoir flow simulation is considered as a compacting nucleus of strain (center of compression; Mindlin, 1936; Geertsma, 1973; Okada, 1992). The contribution of each of these nuclei is integrated to compute the poroelastic stress changes along each fault of the Groningen field with a meter-scale spatial resolution (Figure 2a). The restriction that we presently still have is that only one-way coupling is considered. We deem this acceptable for gas reservoirs, where the effect of compaction on the gas pressures in the pores is small. The Barnes-Hut algorithm (Barnes & Hut, 1986) is used for rediscretizing the initial reservoir grid for two purposes: (i) clustering the nuclei of strain close to the faults in order to increase the spatial stress resolution and (ii) shortening the computation time. The algorithm has been validated by comparison with relatively slow finite-element numerical computations, with excellent results (van Wees et al., 2018). Our approach allows us to quickly resolve the stress changes along each fault of the Groningen field with a meter-scale resolution, while honoring the differential compaction effects due to fault offset. More specifically, it takes 5 hr to compute the depletion-induced stress changes along the 76 faults of the central subarea with a meter-scale spatial resolution (Figure 2a).

We can thus calculate the poroelastic normal and shear stress changes induced by the reservoir compaction for every observation point along each fault (Figure 2b). Observation points are placed on fault pillars (i.e.,

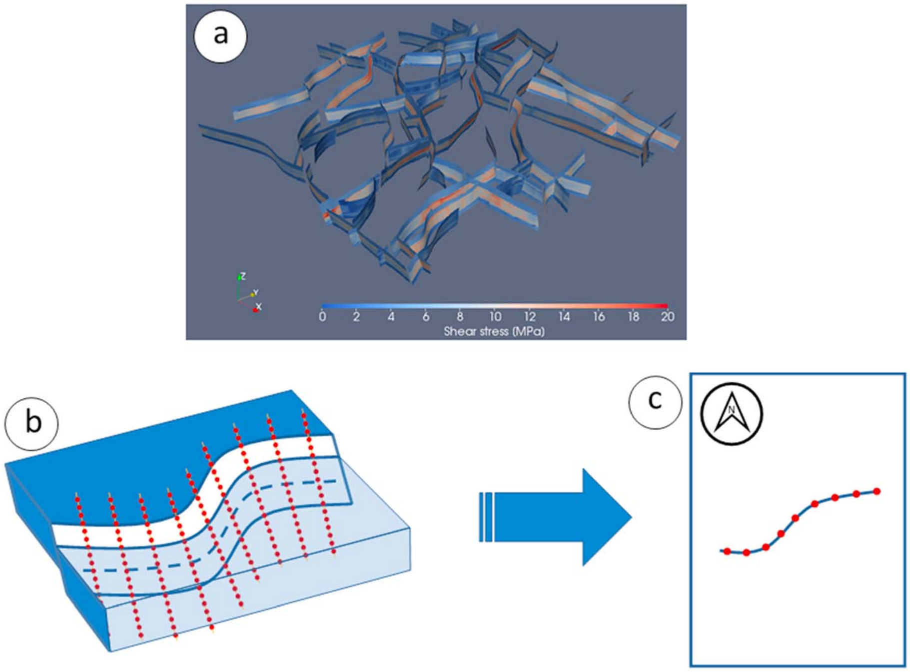

Figure 2. From 3-D to 2-D stress analysis. (a) Example of the fine-resolution 3-D stress (shear stress changes are shown here as example) obtained along faults of the C-area. (b, c) Schematic of the upscaling approach for the 3-D stress components. To map the 3-D geometry (b) onto 2-D fault-curves (c), along each pillar (subvertical lines of red—observation points along the fault dip direction in [b]), we pick the observation point with the highest Coulomb stressing rate (see Appendix A1. for more details).

subvertical lines along the fault dip direction), which in turn make up the 3-D geometry of a fault (Figure 2b). However, we still need to define the pore pressure changes inside the faults to calculate the effective normal stress changes and derive the Coulomb stress changes. For each observation point, the fault pressure is sampled from the reservoir model. This ensures that for each observation point, the corresponding gas or water pressure is used for the stress calculation. In addition, no averaging of pressures between gas and water pressures is used since inside the reservoir no significant two-phase flow is expected. Assuming that the pressure inside the fault is in equilibrium with the surrounding compartments, two endmembers span the range of fault pressure possibilities: a base case scenario in which the fault pressure follows the pressure of the compartment which has experienced the largest pressure change and an alternative scenario in which it follows the compartment with the smallest pressure change. Even though both scenarios have been tested, only the modeling results obtained with the base case scenario are exhaustively detailed in the present manuscript.

Because of the lack of constraint on the depth of the observed events resolution (see more details in section 3.3), the seismicity catalogue can be view as a 2-D field evolving over time. Consequently, for model-data comparison, the model output needs to be represented in 2-D through time as well (Figures 2c and 3). There are a number of ways in which the upscaling from three spatial dimensions to two spatial dimensions can be achieved (Figures 2b and 2c). We decided to represent each fault pillar by its observation point with the maximum Coulomb stressing rate $\dot{S}$. The modified Coulomb stress function is defined as

$$S = \tau - [\mu - \alpha]\sigma_n' \tag{1}$$

with τ is the shear stress acting along the fault plane, σ_n' is the effective normal stress, μ is the coefficient of fault friction, and α is a constitutive parameter (zero in this study). This choice of upscaling approach is supported by the fact that Dieterich's seismicity rate (Dieterich, 1994; defined in section 3.2) is expected to be dominated by the highest positive Coulomb stress changes (Kroll et al., 2017). As presented in Appendix A1. this upscaling approach allows to preserve the temporal dynamic of the seismicity rate modeled in 3-D.

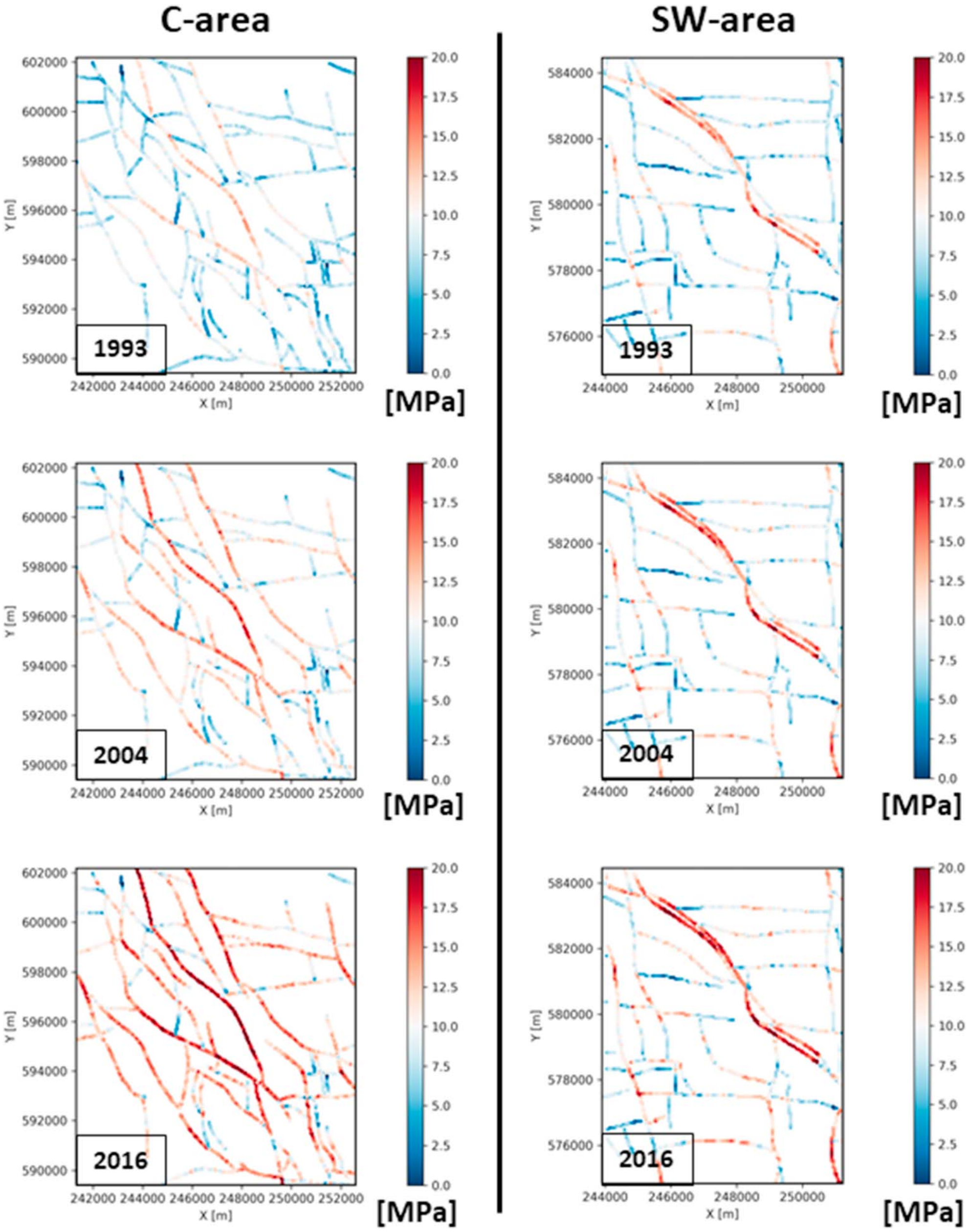

Figure 3. Representative 2-D fault maps obtained after upscaling of the cumulated changes in Coulomb stress for different time steps since the onset of depletion.

2.2. From Stress Rate to Seismicity Rate

The traditional Coulomb failure model predicts that whenever the Coulomb stress reaches a threshold value, an earthquake is generated. Assuming a population of faults on which the prestresses are uniformly distributed up to the threshold value, the Coulomb failure model leads to a direct proportionality between the seismicity rate and the Coulomb stress rate. During any arbitrary stressing history, as soon as the Coulomb stress starts to decrease, the Coulomb failure model predicts an instantaneous shutdown of the seismicity. This prediction is not in agreement with the observed seismicity, which generally shows a gradual decay following the onset of Coulomb stress decrease.

The Coulomb failure model does not honor the frictional constitutive behavior of faults. Laboratory data show that the timing of dynamic instability depends on initial conditions, fault properties, and applied stress (Dieterich & Kilgore, 1996). The rate-and-state friction laws have been established in order to reproduce these laboratory observations (see Marone, 1998, for a review). More specifically, the rate-and-state friction laws reproduce the fact that the onset of frictional sliding is a noninstantaneous time-dependent process (as opposed to the instantaneity assumption of the Coulomb model), which introduces a time-dependent failure mechanism for the generation of earthquakes. Now assuming a population of faults following a rate-and-state frictional behavior and where the time to failure of the nucleation spots along the faults is uniformly distributed, Dieterich (1994) derived the following seismicity rate model:

$$R_D = \frac{r_0}{\gamma \dot{S}_0} \quad \text{where} \quad \frac{d\gamma}{dt} = \frac{1}{A\sigma_n'}\left[1 - \gamma \frac{dS}{dt}\right] \tag{2}$$

where R_D is the seismicity rate, γ is a state variable, and S is the modified Coulomb stress function defined in equation (1). The constant r_0 is the steady-state background seismicity rate at the reference stressing rate $\dot{S}_0$. A is a dimensionless fault constitutive parameter.

Segall and Lu (2015) reformulated this seismicity rate equation to eliminate the state variable γ. They defined a normalized seismicity rate, relative to the background rate, as

$$R = \frac{R_D}{r_0} \tag{3}$$

The differential equation for R, derived from equations (2) and (3), is

$$\frac{dR}{dt} = \frac{R}{t_a}\left[\frac{\dot{S}}{\dot{S}_0} - R\right] \tag{4}$$

where $t_a = A\sigma_n'/\dot{S}_0$ is the characteristic time delay for the earthquake nucleation process, which also corresponds to the time scale of decay of the aftershock rate following a mainshock back to the background rate. Even if the physical meaning of the background stressing and seismicity rates is quite straightforward, the microphysics of the dimensionless fault constitutive parameter A is still debated and other alternatives are proposed like the recent microphysical model formulations of Niemeijer and Spiers (2007) and Chen and Spiers (2016), so called “CNS” model.

Even while changes in σ_n' are accounted for in the computation of the modified Coulomb stress (equation (1)), σ_n' is generally assumed to be constant in $t_a = A\sigma_n'/\dot{S}_0$ (see Rubin & Ampuero, 2007; Segall & Lu, 2015). By fixing σ_n' in t_a, one makes the assumption that the changes in effective normal stress are negligible with respect to the initial effective normal stress and thus do not affect the characteristic decay response of the system. In our context of a depleting gas reservoir, we decided to honor the temporal changes in σ_n' when solving the ordinary differential equation (equation (4)).

Recently, Heimisson and Segall (2018) proposed a modified version of Dieterich's seismicity rate equations (equation (2)) by explicitly accounting for a variable effective normal stress from the start of the derivation. As pointed out by Heimisson and Segall (2018), the difference between their modified version of Dieterich's seismicity rate equations and the original one (equation (2)) is unlikely to be significant unless the effective normal stress change is large. For the training period (1993–2016) the temporal fluctuations of the modeled effective normal stress (during reservoir depletion) are in the range of 3 MPa with an average value $\sigma_n' = 12.5$ MPa. It can thus be expected that using the newly developed equations of Heimisson and Segall (2018) will not lead to a significant departure with respect to the original Dieterich's derivation (equation (2)). All the results presented in the manuscript are thus based on the use of equation (4) but solving the ordinary differential equation accounting for temporal changes in σ_n'.

2.3. The Data: Earthquake Catalogue

Before focusing on the approach for model conditioning, it is important to precisely define the earthquake catalogue used as data. The same earthquake catalogue as used in previous studies (Bourne et al., 2014; Bourne et al., 2018; Bourne & Oates, 2017; Dempsey & Suckale, 2017) and for an identical aim in terms of model conditioning is used in the present approach. This earthquake catalogue has been compiled by the

Royal Netherlands Meteorological Institute (KNMI). Indeed, since at least 1986, KNMI has monitored seismicity in the Netherlands. From the dedicated borehole network deployed since 1995 by KNMI, the magnitude of completeness of the Groningen events is assumed to be $M_L = 1.5$, with a detection threshold of $M_L = 1.0$. The reader is directed toward the work of Dost et al. (2017) where exhaustive details are available on the temporal evolution of the catalogue completeness with the seismic network evolution. We decided here to test the sensitivity of our modeling approach to the minimum magnitude considered. We picked two minimum magnitudes for our analysis: either we restrict our analysis to all events with $M_L \geq 1.0$ or we only select $M_L \geq 1.3$ events.

The seismicity catalogue is essentially a 2-D representation evolving over time, because of the limited depth control on the observed seismicity—except for local results from analyzing deep borehole monitoring clearly showing seismicity that is restricted to the reservoir level (Willacy et al., 2018). Indeed, since the deployment of two downhole monitoring arrays in 2013, most of the hypocentral depths have been inferred to be inside the reservoir within a 50-m depth error (Daniel et al., 2016).

Dost et al. (2012) report an epicentral error of 500 m which is mainly thought to be caused by errors in the velocity model. This 500 m in epicentral errors is similar to the spacing of the network of preexisting normal faults transecting the Groningen field. It is thus difficult to link a particular fault to a particular earthquake. However, after performing a dedicated multiplet analysis, relocated events are found to be located close to existing faults (Jagt et al., 2017). At this level, future seismological modeling approaches will probably benefit from relocated catalogues, but for now we restrict ourselves to the KNMI catalogue since relocated catalogues are still not covering a sufficient spatiotemporal range; for example, the catalogue of Jagt et al. (2017) only gives access to 16 relocated events between 2010 and 2013. In addition, it will be shown in section 4.1 that the spatial resolution of our modeling prediction (~2,000 m) is significantly larger than the epicentral errors of 500 m, suggesting that the density of observed events is the primary limitation on spatial resolution.

One last important information regarding the seismicity catalogue is about the rupture characteristics of the events. For the smallest events it is hard to constrain their focal mechanisms, but for the largest ones, Dost et al. (2012) and Dost and Kraaijpoel (2013) reported normal faulting focal mechanisms which is consistent with the preexisting normal fault offsetting the Groningen reservoir.

2.4. Model Conditioning

Our purpose now is to determine the set(s) of model parameters that give the best agreement between the observed seismicity rate and the computed rate, the so-called *model conditioning* procedure in the sequel.

The model conditioning first requires model results in a 2-D representation. Therefore, we used the upscaled Coulomb stressing rates (one Coulomb stressing rate per fault pillar) to calculate an R_D for each pillar. This calculation was based on Dieterich's theory (equation (4)) with the precomputed histories of Coulomb loading $\dot{S}$ and effective normal stress $\sigma_n^{'}$.

Second, in order to compare the computed rates to the observed seismicity, both uncertainties in model (fault locations and stress calculation) and data (earthquake location) should be accounted for. We thus employed a Gaussian smoothing σ_s to the R_D fields. As a result, the given parameter set to be optimized contains four numbers: ($\dot{S}_0, A, r_0$ and σ_s).

For each set of model parameters the posterior log likelihood is calculated in order to rank the models (Ogata, 1998; Zhuang et al., 2012). The log likelihood is defined as the logarithm of the probability that one specific model (with one specific set of model parameters) has generated the observed earthquake catalog. The best model is the one that gives the maximum log likelihood estimate (MLE). For our nonhomogeneous stationary Poisson process and for a given time interval (t_0, t_1) and spatial area (x_0, x_1) x (y_0, y_1), the log likelihood with respect to N observed earthquakes which have occurred at times t_i and locations (x_i, y_i) is defined by the following function:

$$ll = \sum_{i=1}^{N} \log(R_{D\_\text{smooth}}(xi, yi, ti)) - \iiint_{t0,x0,y0}^{t1,x1,y1} R_{D\_\text{smooth}}(x, y, t)\ \mathrm{d}x\ \mathrm{d}y\ \mathrm{d}t \tag{5}$$

Following a Bayesian approach and because we do not have a prior preference for the shape of the distribution of each model parameter, we attribute a bounded uniform a priori probability distribution for each

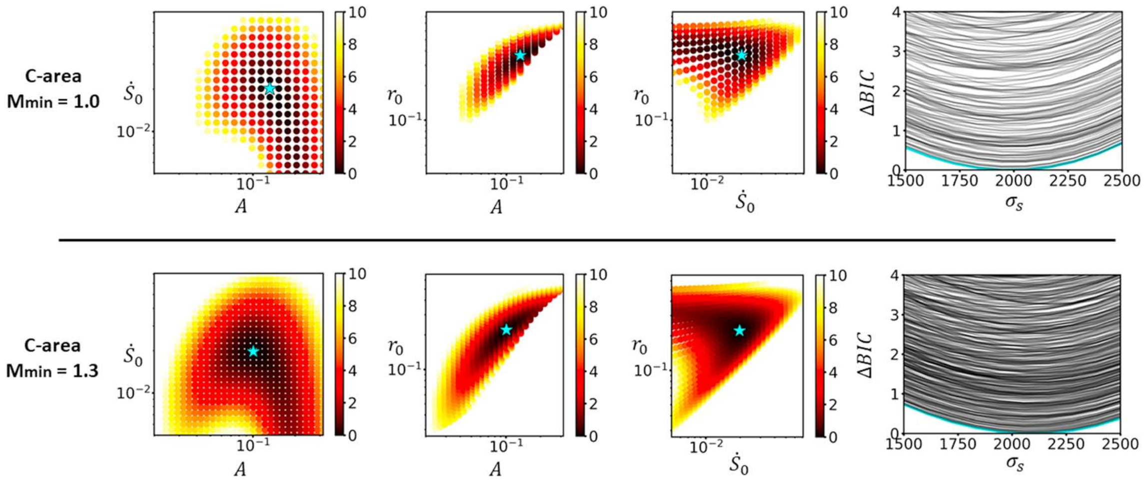

Figure 4. Joint posterior probability distributions of the model parameters of the C-area obtained with the Brute-Force grid search after conditioning during the training period (1993–2011) and for two different values of the minimum magnitude $M_{\min}$ (top: $M_{\min} = 1.0$, bottom: $M_{\min} = 1.3$). The color scales of the scatter plot correspond to differences in Bayesian Information Criterion (ΔBIC) between each parameter sets of the prior distribution and the maximum log likelihood estimate set of parameters (cyan stars). Since the number of observed events and degrees of freedom for all realizations are identical, one can relate the difference in log likelihoods and Bayesian Information Criteria with $\Delta\text{BIC} = 2\Delta LL$.

model parameter. Two methods are used to condition to the data these a priori uniform distributions: (i) a Brute-Force grid search and (ii) MCMC. In the case that the shape of the posterior probability distributions is relatively smooth, both approaches should lead to similar results.

The model conditioning has been pursued over two time periods: (i) from 1 January 1993 to 31 December 2015 (referred as the training period [1993–2016]) and (ii) from 1 January 1993 to 31 December 2010 (referred as the training period [1993–2011]). The two time periods were chosen to enable the identification of temporal changes in the model parameters, if any would exist. Updated model parameters for the training period (1993–2011) have been used to simulate seismicity rates from 1 January 2011 to 31 December 2015 (referred as the forecast period [2011–2016]) and to assess the forecast capability of our modeling approach.

3. Results

We selected two subareas, which we will call the Central area (C-area) and the Southwest area (SW-area). These areas represent two contrasting temporal earthquake activity dynamics (Figure 1): the overall seismicity rate in the C-area is higher than in the SW-area. This approach offers the opportunity to (i) explore the dynamics with a higher spatial and temporal resolution, (ii) capture possible spatial variations, and (iii) assess the robustness and versatility of our modeling approach. This is an advantage compared to previous attempts based on modeling at the scale of the entire Groningen field (Bourne et al., 2014; Bourne et al., 2018; Bourne & Oates, 2017; Dempsey & Suckale, 2017).

3.1. Comparison of Posterior Model Parameters Between the High and Low Seismicity Areas

As mentioned previously, we chose two minimum magnitudes for our analysis: either $M_L \geq 1.0$ or $M_L \geq 1.3$. Interestingly, we found similar posterior probability distributions of the rate-and-state parameters and similar MLE for these choices (Figure 4). This proves the robustness of the spatiotemporal distribution of the events with respect to the range of magnitudes considered.

For the two search approaches we followed, Brute-Force and MCMC, similar results were obtained for the median of the posterior distributions (Figures 4 and 5). Following a rather coarse grid search, we can match the optimized MCMC grid search. We interpret this result as a direct consequence of the smoothness of the log likelihood function (equation (5)) in our case.

For the high-seismicity C-area, the marginal posterior probability distributions of each model parameter obtained after conditioning with the data over all the training periods are well constrained (Figure 5). The distributions obtained after conditioning with each training period are similar (Figure 5). However, for

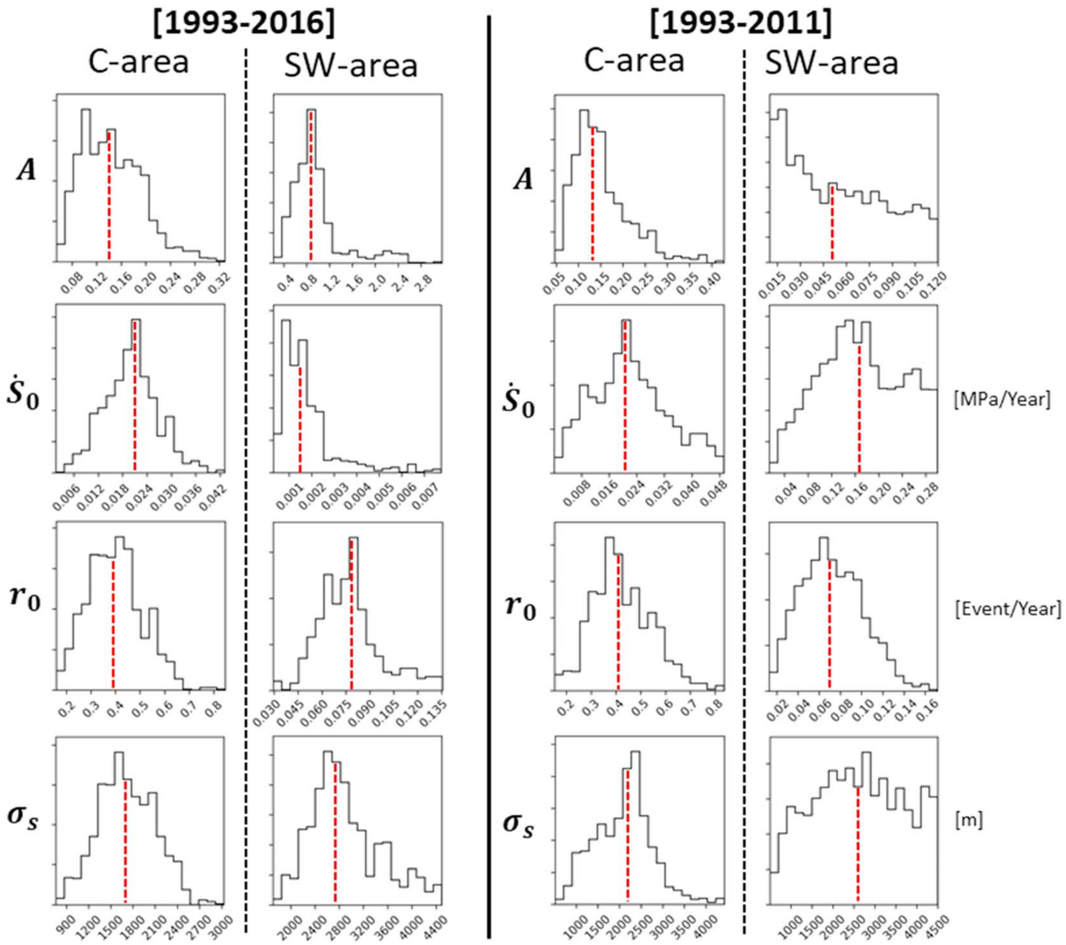

Figure 5. Marginal probability distributions of model parameters obtained with the Markov Chain Monte Carlo search (with a minimum magnitude of 1.0) for both subareas of interest and for the two considered training periods (indicated by labels on top). Bounded uniform prior distributions for each model parameters are A: $\mathbf{U}(1e^{-3}, 10)$, $\dot{S}_0$: $\mathbf{U}(5e^{-6}, 0.5)$, r_0: $\mathbf{U}(5e^{-4}, 5)$, σ_S: $\mathbf{U}(500, 4{,}500)$—with $\mathbf{U}$(a, b) is a uniform distribution between a and b.

the low-seismicity SW-area only the marginal posterior probability distributions obtained after conditioning with the training period (1993–2016) are well constrained. Clearly, during the period (1993–2011), the low number of observed events in the SW-area precludes constraining the model parameters. The number of events was much larger in the period (1993–2016), thanks to the burst of events recorded in 2014 in the SW-area. The temporal increase of the data information density can be visualized in the update of the standard deviation σ_s of the Gaussian smoother. The posterior distribution of σ_s becomes constrained, and its median decreases when conditioning with the training period (1993–2016). As pointed out by Bourne and Oates (2017), in our modeling approach most of the spatial uncertainties are probably attached to the relatively low number of observed events, since the location error (500 m) is significantly smaller than the length scale σ_s of the Gaussian smoother. Consequently, increasing the duration of the training period results in increasing the number of observed events in the SW-area, and in return the smoothing length scale σ_s decreases.

The best posterior estimates (i.e., the median of the marginal posterior distributions) of the model parameters after conditioning during the training period (1993–2016) are quite different for the C-area and the SW-area (Figure 5). This reveals the spatial heterogeneity of the rate-and-state parameters over the Groningen field.

Both the background stressing rate $\dot{S}_0$ and seismicity rate r_0 are much lower in the SW-area ($\dot{S}_0 = 0.0015$ MPa/year, $r_0 = 0.075$ event/year) compared to those estimated for the C-area ($\dot{S}_0 = 0.02$ MPa/year, $r_0 =$

0.4 event/year). The fact that both background parameters follow the same decreasing trend from the C-area to the SW-area reveals their interindependency, as pointed out by Catalli et al. (2008).

The frictional parameter A is significantly higher for the SW-area ($A = 0.8$) compared to the one estimated for the C-area ($A = 0.14$). Interestingly, Hunfeld et al. (2017) recently performed frictional laboratory experiments on reservoir rock samples from the C-area. Our estimate of A for the C-area is 1 order of magnitude higher compared to the value of 0.01 derived from the laboratory experiments of Hunfeld et al. (2017). However, since in Dieterich's seismicity rate equation the parameter A is only involved via its product with the effective normal stress $\sigma_n^{'}$, one should compare estimates of the joint frictional resistance $A\sigma_n^{'}$. In our Groningen modeling, the average effective normal stress is 12.5 MPa during the training period (1993–2016), leading to $A\sigma_n^{'} = 1.7$ MPa. Hunfeld et al. (2017) performed their frictional experiments with an effective normal stress of 40 MPa, leading to $A\sigma_n^{'} = 0.4$ MPa. Interestingly, both values of frictional resistance $A\sigma_n^{'}$ are in the same range. The difference in A between our modeling and the laboratory experiment is thus partially compensated by the difference in effective normal stress.

Differences in the rate-and-state model parameters lead to a characteristic relaxation time of seismicity, $t_a = A\sigma_n^{'}/\dot{S}_0$, significantly longer in the SW-area (t_a=6,700 years) than in the C-area (t_a=87 years).

3.2. An Unsteady Fault System

As in previous studies of the Groningen-induced seismicity (Bourne et al., 2014; Bourne et al., 2018; Bourne & Oates, 2017; Dempsey & Suckale, 2017), our analysis period starts in 1993 when a significant earthquake activity started to be recorded. In doing so, Dieterich's seismicity rate equation (4) is solved assuming initial condition at steady state, that is $R(0)= 1$ in 1993. However, reservoir production at Groningen started in 1968 and given the relatively long t_a inferred from our analysis, it is most likely that the background activity was not at steady state in 1993. In fact, defining $R^{'} = \beta R$ and by operating a change of variable, we can show that $R^{'}$ satisfies an equation similar to equation (4) and reads

$$\frac{\mathrm{d}R^{'}}{\mathrm{d}t} = \frac{R^{'}}{A\sigma_n^{'}/\dot{S}_0^{'}}\left[\frac{\dot{S}}{\dot{S}_0^{'}} - R'\right] \tag{6}$$

with the unsteady initial condition $R'(0) = \beta$ in 1993 and the background stressing rate $\dot{S}_0^{'} = \dot{S}_0/\beta$. Following equation (3), this solution corresponds to a background seismicity rate $r_0^{'} = r_0/\beta$. This mathematical derivation implies that the background stressing rate $\dot{S}_0^{'}$ and background seismicity rate $r_0^{'}$ were $1/\beta$ times lower in 1968, at the start of production when the system was steady, compared to the values of $\dot{S}_0$ and r_0 inferred for 1993 in section 4.1. The latter cannot be interpreted as real steady-state background values (before reservoir depletion) but should be understood as “apparent background values” which are actually the reference values at the initial time of the analysis, here 1993. More precisely, r_0 is the (real) seismicity rate $R_D(0)$ at the beginning of 1993 and $\dot{S}_0$ is the (virtual) Coulomb steady stressing rate that would make the seismicity steady at the rate r_0. Note that $\dot{S}_0$ is not the same as the real Coulomb stressing rate $\dot{S}(0)$ at the beginning of 1993. It is an important aspect of our case study that the Groningen fault system was probably never at steady state since the start of production. During this transient phase and for the two subareas selected for our analysis, the fault system is *in transition* between its initial steady state before the start of production and the next steady-state phase. During this transient phase, due to the Groningen depletion, the *apparent* background stressing rate and background seismicity rate are constantly increasing. However, it is important to note here that the fault constitutive parameter A is expected to remain constant in time.

3.3. Temporal Patterns: Long-Period Fluctuations

From the posterior density distributions obtained with the MCMC search one can randomly pick an ensemble of posterior predictions to visualize its spread and compare it with the data (see Figures 6a and 6d). Both ensembles (C-area and SW-area) of posterior predictions obtained after conditioning with the training period (1993–2016) capture very well the low-frequency temporal fluctuations of the observations. It is also important to point that the fast response of the seismicity rate after the 2014's production rate reduction imposed by the Dutch government (e.g., De Waal et al., 2015; Muntendam-Bos et al., 2017; van Wees et al., 2018) is also well predicted by our approach.

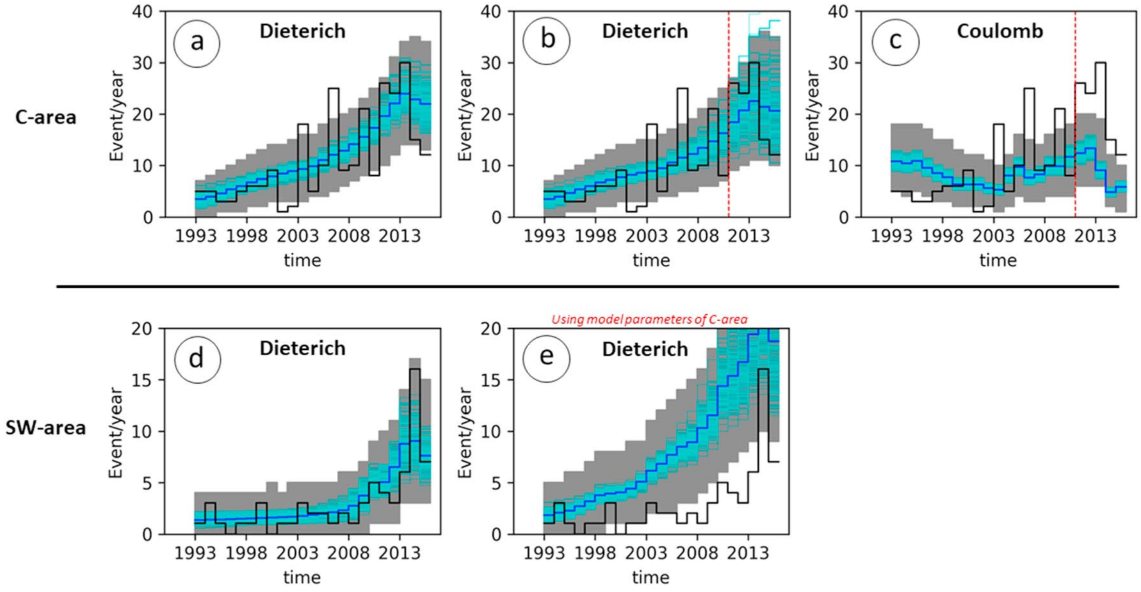

Figure 6. Comparison of the predicted seismicity histories (annual event rate) with the data (dark). The model corresponds to 300 realizations (cyan) randomly drawn from the posterior density distribution obtained with the Markov Chain Monte Carlo search during calibration and with a minimum magnitude of 1.0. The mean of the models is displayed in blue. The gray region indicates 95% of the distribution when stochastic Poisson variabilities are accounted for. For each posterior member, 30 synthetic catalogues are generated in order to account for stochastic Poisson variabilities. The gray region indicates 95% of the distribution of the 9,000 synthetic catalogues. The top and bottom rows correspond, respectively, to the results obtained with the C-area and SW-area. For (a), (d), and (e) the training period is (1993–2016). For (b) and (c) the training period is (1993–2011) and model predictions are propagated up to 2016. The red vertical dashed line indicates the end of the training period (2011). Results of the Coulomb failure model (later discussed in section 4.7) are presented in (c). This spread of the Coulomb modeling approach is clearly not capable of capturing the data in dark. This is even more clear over the forecast period. In (e), the seismicity rate of the SW-area is predicted using the posterior model parameters of the C-area and the stress history of the SW-area; the substantial difference between this model and the observed seismicity demonstrates that the difference between the inferred model parameters of both subareas is significant.

The ensemble of posterior distributions for the C-area obtained by conditioning during the training period (1993–2011) has been used to propagate our simulations up to 2016 (Figure 6b). The median of this propagated ensemble of realizations is very similar to the median of the posterior ensemble obtained with model parameters conditioned over the period (1993–2016). As noted before, this last result indicates that the data during the period (1993–2011) are already informative enough to constrain the model parameters of the C-area.

3.4. Temporal Patterns: Short-Period Fluctuations

The very high frequency temporal changes of the observed seismicity rate, that is, fluctuations with characteristic time scales shorter than about 1 year, are partially missed by our modeling approach. For example, in Figure 6a (C-area), observed bursts of seismicity in 2003, 2006, and 2009 are outside the uncertainty band due to Poissonian stochasticity. The limitation of the temporal model predictions at high frequency, also observed in the previous seismological models of the Groningen seismicity (Bourne et al., 2014; Bourne & Oates, 2017; Dempsey & Suckale, 2017), might be attributed to the fact that we used the yearly sampled pressure fields from the reservoir simulations. In doing so, the seasonal swing of the gas production (high production rate during the winter and low production rate during the summer) is missed (Figure 7b; Nepveu et al., 2016; Sijacic et al., 2017; Hettema et al., 2017). One can thus ask the legitimate question: Can the high-frequency (seasonal) fluctuations of production rates help explain the observed seismicity spikes? Ideally, our modeling approach should be applied with monthly sampled pressure and monthly sampled stressing to recalculate seismicity histories. Instead, a synthetic test is presented here in order to give first hints on the expected effect of the seasonal production swing on the Groningen seismicity.

Figure 7a presents the average-induced stressing rate of the C-area during the training period (1993–2016); this is the yearly sampled stressing rate used in our modeling approach. The missing part of the puzzle, presented in Figure 7b, is the monthly production of the Groningen field, which gives hints on the expected

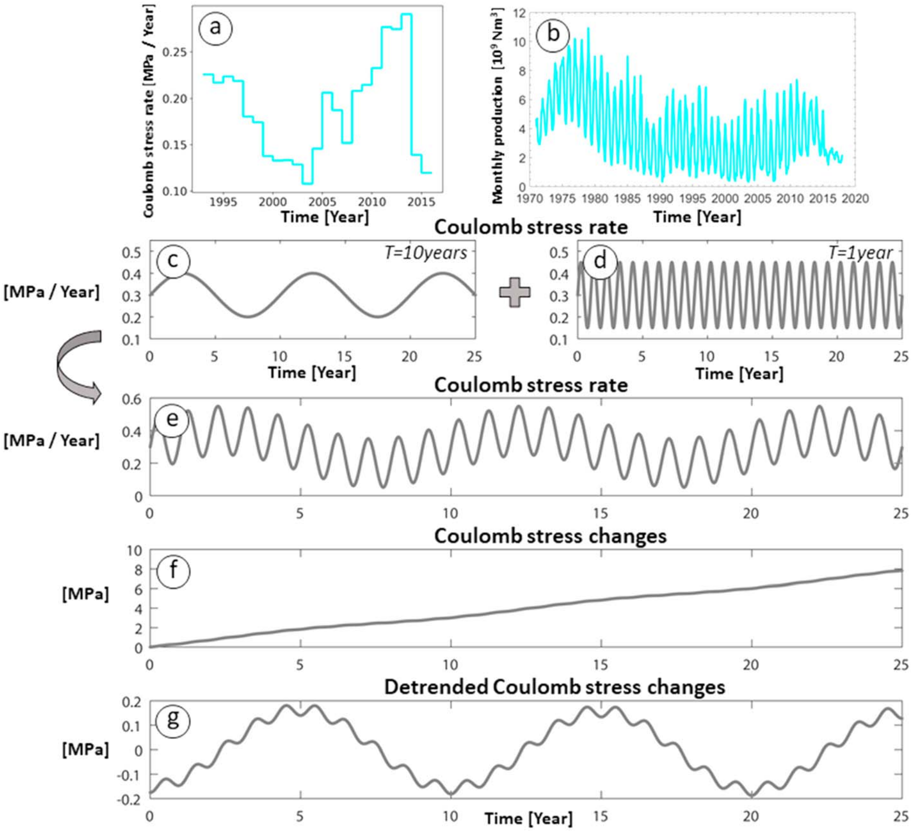

Figure 7. Synthetic approximation of the monthly sampled stressing history. (a) Yearly stress rate of the C-area calculated from the yearly pressure fields. Because of the yearly sampling, this stress profile only presents long-period fluctuations of roughly 10-year period. (b) Monthly production rate of the Groningen field, revealing seasonal fluctuations with amplitude as large as that of the long-period fluctuations. (c, d) Synthetic approximation of the stress history of the C-area, modeled as two harmonics of same amplitude equal to the one modeled in our study based on yearly pressure fields. (e, f, g) Recomposed biharmonic synthetic stress profile.

stressing history if we would have modeled it with monthly sampled pressure fields. The time delay between production changes at wells and stress changes at faults due to pressure diffusion is disregarded, since in our approximation the exact timing of the harmonic stress perturbations does not matter but it is rather the relative timing between stress perturbations and seismicity at faults which is of main interest. The expected stressing history can thus be decomposed into two harmonics (Figures 7c–7e): (1) the roughly 10-year long-period fluctuations already captured in our modeling approach and (2) the 1-year short-period fluctuations due to the seasonal production swing.

Before moving forward in the argumentation, it is important to note that the amplitudes of the 1-year period fluctuations of the monthly field production are as large as the long-period ones (Figure 7b). The stress rate fluctuations are thus expected to follow the same trend; that is, both short- and long-period stress rate fluctuations are expected to be of same amplitude (Figures 7c–7e). Because the amplitude of stress changes is related to the product of amplitude and period of stress rate fluctuations, the amplitude of the stress changes due to the 1-year harmonic is expected to be significantly smaller compared to the one generated by the 10-year harmonic (see Figures 7f and 7g).

It is already well known (see Ader et al., 2014; Beeler & Lockner, 2003; Lockner & Beeler, 1999) that Dieterich's seismicity model predicts two different behaviors of the seismicity response depending on whether the period of the perturbation T is larger or smaller than the characteristic period T_a defined as

$$T_a = 2\pi\, t_a \tag{7}$$

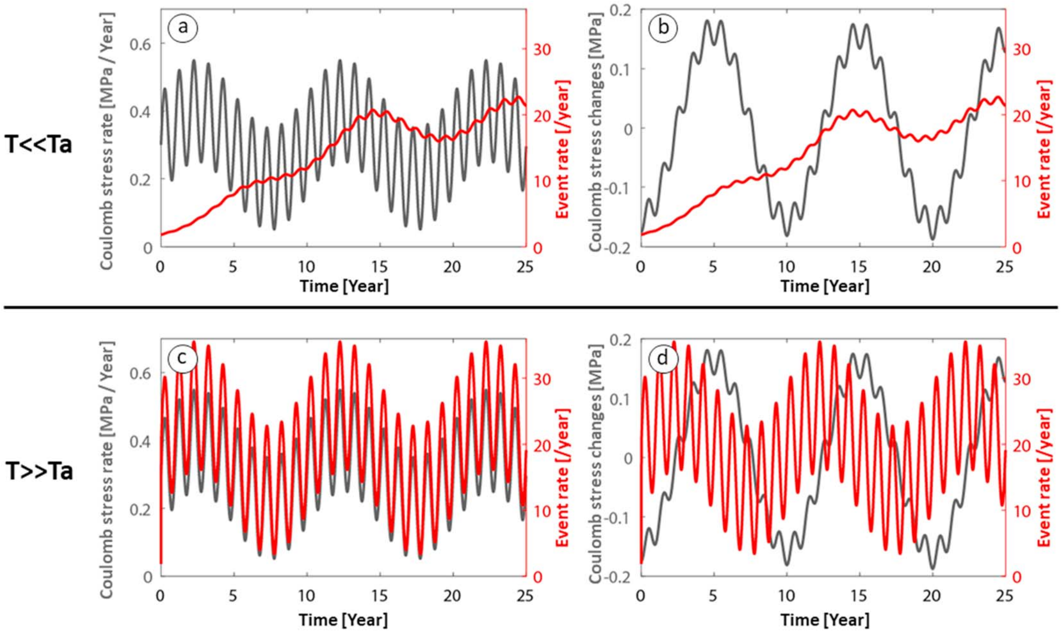

Figure 8. Rate-and-state seismicity response to the biharmonic stress perturbations (T = 10 years and T = 1 year) of the C-area. Top row (a, b) The characteristic period T_a corresponds to the one derived in our study for the C-area, that is, T_a = 547 years with t_a= 87 years. In this regime, where $T \ll T_a$, the seismicity rate is proportional and in phase with the Coulomb stress change. The low-amplitude seasonal stress fluctuations lead to low-amplitude seismicity rate fluctuations. Note here the Coulomb stress change time series (b) is detrended as in Figure 7g. Bottom row (c, d) An arbitrary very short characteristic period $T_a = 0.2$ year (and in opposition with our modeling results) is needed for the seismicity response to be proportional to the stressing rate and to generate high-frequency bursts of seismicity.

For short perturbation periods such that $T \ll T_a$, the variations of the seismicity rate are proportional to and in phase with the Coulomb stress *change*. For long perturbation periods such that $T \gg T_a$, the variations of induced seismicity rate are proportional to and in phase with the Coulomb stress *rate* (Ader et al., 2014).

This seismicity rate response to harmonic perturbations assumes that the fault system is at steady state (Ader et al., 2014). It remains to be shown that the same seismicity response to harmonic perturbations still holds for an unsteady fault system, as is the case for Groningen. This is demonstrated in Appendix A2. with the difference that the characteristic time scale controlling the spectrum of the sensitivity to stress perturbations is now

$$T_a(t) = 2\pi\, t_a(t) \tag{8}$$

where

$$t_a(t) = \frac{a\sigma_n^{'}}{\dot{S}_u(t)} \tag{9}$$

and $\dot{S}_u(t)$ is the long-term-induced Coulomb stressing rate history in the absence of seasonal stress fluctuations. In particular, the effective t_a is now time dependent, it changes with the evolving background stressing rate (i.e., the long-term Coulomb stressing rate) as presented in section 4.2. In our analysis, we derived, during the unsteady state, an effective t_a(1993)=87 years for the C-area. The shorter t_a the system could reach at the new steady state (*ss*) equals the long-term-induced Coulomb stressing rate at Groningen; that is, $\dot{S}_u = 0.3$ MPa/year and t_a(*ss*)=5.83 years. In consequence, both the 1- and 10-year perturbation periods are shorter than the range of characteristic time scales T_a (547 years − 37 years) controlling the seismicity rate response. In this situation, and as displayed in Figures 8a and 8b, the variations of the induced seismicity rate are proportional to and in phase with the Coulomb stress change. In our case, since the amplitude of the stress changes due to the 1-year harmonic is small, the 1-year period seismicity rate fluctuations are also of low amplitude (see Figures 8a and 8b). We conclude that our modeling approach rejects the hypothesis of

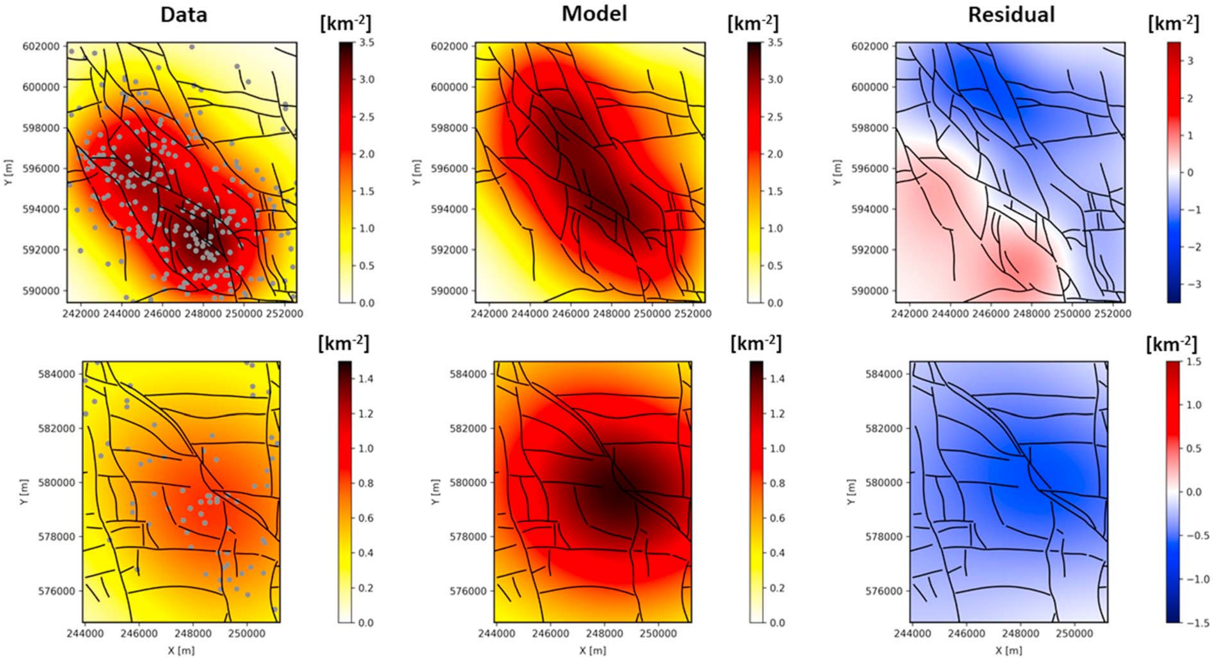

Figure 9. Comparison of the spatial pattern of the models and data event density during the training period (1993–2016) for the C-area (top row) and SW-area (bottom row). The residual map is the difference between data and model.

causality between the seasonal swing of the gas production and the observed seismicity spikes. Interestingly, since the effective t_a shortens over time, the model predicts that for the two selected subareas the Groningen system is progressively more responsive to the stressing rate. This is visible in Figures 8a and 8b where the amplitude of the seismicity rate fluctuations, either at 1-year period or 10-year period, progressively increases through time.

For illustrative purposes, we also present in Figures 8c and 8d the hypothetic regime of long perturbation periods such that $T \gg T_a$, with $T_a(1993) = 0.2$ year. In this case, both harmonic stress perturbations, of identical stress rate amplitude, lead to seismicity rate fluctuations of identical amplitude. This regime requires extremely short t_a which is (i) incompatible with our modeling results and (ii) would predict fast seismicity response at the onset of depletion in contradiction with the observations.

3.5. Spatial Patterns

Another way to assess the performance of our modeling approach is to compare the observed and modeled spatial distribution event density during the period (1993–2016) (see Figure 9). For the C-area, a region of high event density is localized along the diagonal NW-SE for both data and model. The fault density along this diagonal is also the highest. However, it is important to note, as an example, that in the Northeast part faults are still mapped but our approach successfully predicts less seismicity along these faults, consistent with observations. In our modeling approach, the local combination of (i) a less severe pressure depletion and (ii) nonoptimally oriented faults for depletion-induced stress changes (see Figure 3) can explain the lower seismicity level in the Northeast part of the C-area. For the SW-area, even if faults are uniformly distributed, interestingly, only a distinct small spot of high event density appears at the same location for both data and model. Nonetheless, for both subareas residuals remain between data and model event density fields; factors that might contribute to these spatial mismatches will be discussed in section 5.

3.6. Insignificant Effect of Aftershocks

One of the highly debated assumptions of Dieterich's seismicity rate theory (Dieterich, 1994) is the lack of interactions between seismic sources. More specifically, Dieterich's seismicity rate theory (Dieterich, 1994) assumes that aftershocks are directly triggered by the stress changes induced by their mainshock; but the effect of stress interactions between aftershocks is not honored. However, as demonstrated by Ziv and Rubin (2003) this assumption is not as limiting as it seems at first glance, because interevent stress interactions affect not only the transient stressing history but also the effective background stressing rate. On the one hand, interevent interactions trigger more aftershocks, which tend to prolong the duration of the aftershock sequence. On the other hand, the enhanced triggering increases the background stressing rate, which tends to shorten the aftershock sequence duration. The two effects counteract each other, and the aftershock duration predicted by Dieterich's theory remains unchanged. Very recently, Heimisson (2019) has proposed a revisited version of Dieterich's seismicity rate theory (Dieterich, 1994) which accounts for source interactions and confirms the earlier findings of Ziv and Rubin (2003).

We could further examine the effects of interevent interactions in our modeling framework, by (1) following the new version of Dieterich's theory accounting for interactions recently implemented by Heimisson (2019), (2) using the Epidemic-Type Aftershock Sequence (ETAS) model (Ogata, 2011), or even (3) declustering the earthquake catalogue, that is, performing a statistical separation into background (i.e., mainshocks directly induced by gas depletion) and clustered populations (i.e., aftershocks). It is important to point here that for these three alternatives, stress transfers between aftershocks are not explicitly modeled. In addition, the cluster properties can be affected by various catalogue uncertainties. In particular, increased earthquake location errors can lead to artificially increased either clustering or background rates (see, e.g., Zaliapin & Ben-Zion, 2016).

We could couple Dieterich's seismicity model with ETAS (see, e.g., Llenos & McGuire, 2011): The former would provide the event rate of the independent main events, the latter the aftershock productivity. The ETAS model has been recently used in the context of induced seismicity (Llenos & Michael, 2013) and even for the Groningen field (Bourne et al., 2018). We decide here to apply the declustering algorithm of Zaliapin et al. (2008) and Zaliapin and Ben-Zion (2016), which resolves complete triggering chains based on the relative space-time-magnitude distances introduced by Baiesi and Paczuski (2004). Details of the method and results are presented in Appendix A3.. For the SW-area, over a total of 67 events, only three events are identified as clustered aftershock events. For the C-area, 39 clustered aftershocks and 219 mainshocks are identified; that is, approximately 18% of the events are aftershocks. Applying the ETAS model over the whole Groningen field, Bourne et al. (2018) found an aftershock proportion of 10–15%. We then reestimate the parameters of Dieterich's model with the declustered catalogues (see Appendix A3. for figures). Only the C-area is presented here, since removing the three clustered events of the SW-area is not expected to change the model parameters. The posterior density distributions of each model parameter of the C-area are almost identical to the ones derived with the original catalogue. It is thus a reasonable approach to apply Dieterich's seismicity rate theory over the original catalogue including aftershock events.

3.7. Predictive Performance

This section is dedicated to assess the forecast capacity of our model over the forecast period (2011–2016) when the model parameters have been solely conditioned with the training period (1993–2011). We focus on the C-area, since for the low-seismicity SW-area only the posterior model parameters obtained after conditioning with the training period (1993–2016) are well constrained.

To formally judge the predictive capacity of our model, we perform a number of Regional Earthquake Likelihood Model tests on the model forecasts. For this purpose, we forecast event rates for the period (2011–2016) based on the maximum a posteriori estimate of the model parameters determined for the training period (1993–2011). Since the model parameters are fixed for the forecast period, the forecast model has no degrees of freedom.

The first test, the *N*-test, tests the consistency of the model with the data (Schorlemmer et al., 2007), that is, how well the forecast number of earthquakes (the model) matches the observed number of events (the data). The analytical form followed by Zechar et al. (2010) is used here as

$$\delta_1 = 1 - F((N_{\mathrm{obs}} - 1) | N_{\mathrm{fore}}) \tag{10}$$

$$\delta_2 = F(N_{\mathrm{obs}} | N_{\mathrm{fore}}) \tag{11}$$

where $F(x|\mu)$ is the right-continuous Poisson cumulative distribution function with expectation μ evaluated at x and $F(x|\mu) = 0$ for all $x < 0$. To be clear, δ_1 is the probability of observing at least N_{obs} earthquakes, given

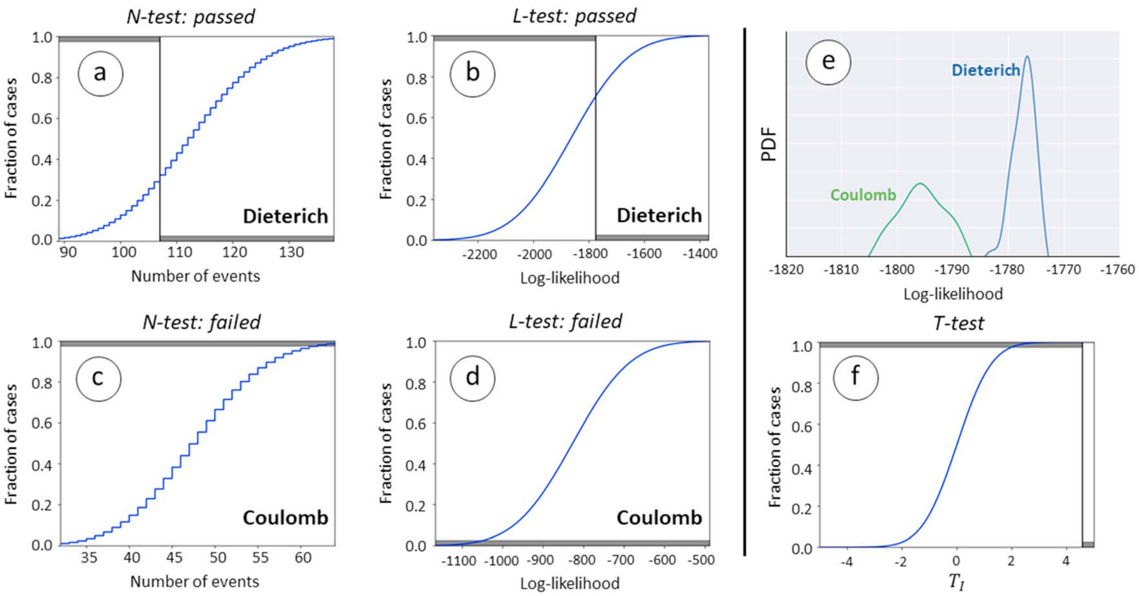

Figure 10. Forecast performance results within the C-area for models trained over the period (1993–2011) and tested over the period (2011–2016). (a; c) *N*-test for the Dieterich and Coulomb models, respectively. The vertical line indicates the number of observed events; the blue line is the cumulative distribution of the number of expected events in the forecast. The gray areas indicate the rejection bars. Since the blue line does not intersect the gray bars for the Dieterich model (a), the forecast is considered to be consistent with the data. Instead, the Coulomb model (c) failed this test. (b, d) *L*-test for the Dieterich and Coulomb models, respectively. The vertical line indicates the log likelihood of the observed events; the blue line is the cumulative distribution of log likelihoods of simulated catalogues conforming to the forecast. The gray areas indicate the rejection bars. Since the blue line does not intersect the gray bars for the Dieterich model (a), the forecast is considered to be consistent with the data. Again, the Coulomb model (c) failed this test. (e) The Probability Distribution Function (PDF) of log likelihoods of the observed events is significantly lower for the Coulomb failure model. (f) *T*-test: information gain per sample (per observed event) of the Dieterich model over the Coulomb model. The blue line is the t_{N-1} cumulative distribution function. Since $|T_I|$ (the dark vertical line) falls well within the extreme tail of the t_{N-1} distribution, the Dieterich model (with the higher log likelihood) outperforms the Coulomb model.

that N_{fore} are expected; δ_2 is the probability of observing at most N_{obs} earthquakes, given that N_{fore} are expected. In our case, $N_{\text{fore}} = 112.6$ and $N_{\text{obs}} = 107$, equations (10) and (11) yield, respectively, $\delta_1 = 0.71$ and $\delta_2 = 0.32$. Both δ_1 and δ_2 are superior than the critical value of $\delta_{\text{eff}} = 0.025$ in order to maintain a Type I error of $\alpha = 5\%$; thus, the observation is consistent with the forecast. In other words, the forecast contains on average 112.6 events of magnitude 1.0 and higher, while the data contain 107 such events. Synthetic catalogues based on the forecast would contain a number of events drawn from a Poisson distribution with an expected value of 112.6. Of these catalogues, 95% would contain between 92 and 133 events. Since the number of observed events ($N_{\text{obs}} = 107$) falls within the acceptable range under the given $\alpha = 5\%$, the model and the data are thus consistent (Figure 10a).

The second test, the *L*-test, checks whether the observed likelihood of the model (the likelihood score obtained when using the observed events) is consistent with the expected distribution of likelihood scores from this model (Schorlemmer et al., 2007). Synthetic catalogues based on the forecast can be evaluated against the forecast that created them. This gives an expected distribution of likelihood scores of catalogues conforming to the forecast. This expected distribution of likelihood scores can also be obtained analytically (Rhoades et al., 2011). Based on the forward model, 95% of the catalogues would have a log likelihood between −2,187.88 and −1,540.05. Since the log likelihood of the observed events (−1,775.3) falls within this range, the model and the data are consistent (Figure 10b).

Finally, we compare Dieterich's model to the Coulomb failure model (Figure 6c) which predicts the following instantaneous direct relationship between stressing rate $\dot{S}_f$ and seismicity rate R_c

$$\frac{R_c}{r_0} = \frac{\dot{S}_f}{\dot{S}_0} \tag{12}$$

where $\dot{S}_f$ denotes the positive part of the Coulomb stressing rate, since negative seismicity rates are excluded (Ader et al., 2014). The distribution of the log likelihoods of the observed events during the forecast period

(2011–2016) for the posterior ensemble of models trained during the period (1993–2011) is significantly worse for the Coulomb failure model (Figure 10e). This result is further confirmed by the Coulomb model failing both the N-test and the L-test over the forecast period (2011–2016; Figures 10c and 10d).

As a way to compare the performance of two models, a third last test can be used, the T-test (Rhoades et al., 2011), which gives the information gain per sample (per observed event) of model A over model B

$$I_N(A,B) = \frac{1}{N}\sum_{i=1}^{N}(X_i - Y_i) - \frac{N_{\text{fore}A} - N_{\text{fore}B}}{N_{\text{obs}}} \tag{13}$$

where $X_i = \log\left(R_A(xi, yi, ti)\right)$ and $Y_i = \log\left(R_B(xi, yi, ti)\right)$. The expected value for information gain per sample for equally performing models is zero. In order to test whether or not the information gain per sample differs significantly from zero, the students t-distribution with $N_{\text{obs}} - 1$ degree of freedom (t_{N-1}) is used. Indeed, for the information gain per sample to differ significantly from zero, the absolute value of the normalized information gain $T_I = I_N(A,B)/\left(s/\sqrt{N}\right)$ should fall in the extreme tail of the t_{N-1} cumulative distribution function, where s denotes the sample variance of $X_i - Y_i$ and defined as

$$s^2 = \frac{1}{N-1}\sum_{i=1}^{N}(X_i - Y_i)^2 - \frac{1}{N^2 - N}\left(\sum_{i=1}^{N}(X_i - Y_i)\right)^2 \tag{14}$$

In our scenario, models A and B correspond, respectively, to Dieterich's model and the Coulomb model. $|T_I| = 4.58$ falls well within the extreme tail of the t_{N-1} distribution (see Figure 10f), confirming that (i) the performance of Dieterich's model and Coulomb's model are statically significantly different and (ii) the Coulomb model (with the lower log likelihood) can be rejected in favor of Dieterich's model.

4. Discussion and Conclusions

We presented a Coulomb rate-and-state modeling approach including most of the key ingredients acting in concert in the generation of induced events during the gas production of the Groningen field. The ingredients include (i) details of the spatiotemporal pressure distribution from reservoir simulations, (ii) poroelastic effect of the reservoir contraction accounting for the differential compaction between compartments bounded by faults with offsets, and (iii) Dieterich's seismicity rate theory (Dieterich, 1994) incorporating the effective frictional response of a population of faults. We showed that the model parameters of both selected subareas of the Groningen gas field can be constrained by the data covering the period (1993–2016) and that the first-order spatiotemporal distribution of the observed seismicity is captured by our modeling approach. Due to the difficulties to constrain the model parameters of the SW-area over the training period (1993–2011), solely the forecast capacity of the C-area has been assessed over the period (2011–2016). Our modeling approach over the C-area successfully passed a series of predictive performance tests, and it has been demonstrated that Dieterich's seismicity theory outperforms the traditional Coulomb failure model.

Three main ingredients should be carefully handled in the modeling of induced seismicity: (1) the data, (2) the forward modeling, and (3) the stochastic Poisson variabilities. Each of these ingredients, if not properly honored, might contribute to the remaining mismatch between the predicted and observed seismicity.

For example, our modeling of the Groningen-induced seismicity, coupling Coulomb stressing rate with Dieterich's theory, does not include the intrinsic Poisson variability of earthquakes occurrence. The observed catalogue is considered here as one unique realization of a stochastic, nonstationary Poisson process, and each posterior member of our modeling approach is one particular model of the time-dependent seismicity rate underlying the Poisson process. Consequently, before any data-model comparisons, one should account for stochastic Poisson variabilities. This is realized by creating synthetic catalogues through Monte Carlo simulation following Zhuang and Touati (2015). For each posterior member, which can be considered as the mean of an underlying Poisson distribution, multiple synthetic catalogues are generated where the likelihoods of the event location and timing are proportional to the event density. The gray regions in Figure 6 bound 95% of the ensemble of these stochastic realizations. Without considering stochastic Poisson variabilities, the model underestimates the event rate reduction of the C-area after the production rate reduction in 2014. Including Poisson variabilities, the large reduction of the observed event rate falls inside the range of the posterior distribution. However, and as discussed before, some very high frequency fluctuations of the observed seismicity rate are outside the uncertainty range due to Poissonian stochasticity. One can thus attribute the model-data mismatch to the two other ingredients, either to the data or to the forward modeling.

Regarding the data, the spatial error of the event locations might not be well constrained; for example, its temporal evolution with the improvement of the seismic network should be accounted for in future work. Regarding the forward modeling, a more precise modeling would involve monthly sampled stress fluctuations of the Groningen field. We do not expect that the rate-and-state theory, with the model parameters inferred in this study, can explain the triggering of the observed bursts of seismicity by the seasonal swing. However, one cannot exclude the possible effect of high-frequency poroelastic stressing which would be missed by our yearly analysis. Another candidate to explain these bursts might be the presence of aftershock sequences. We have shown that it is not the case and that Dieterich's neglect of interevent interactions is appropriate, which justifies our use of the original catalogue including clustered events.

Finally, still at the forward modeling level, several other potential candidates might contribute to the remaining mismatch between the predicted and observed spatial event densities: (1) the fault pressure evolution is not properly modeled; (2) the reservoir compaction is not properly modeled; for example, its potential inelastic component (Pijnenburg et al., 2018) is not accounted for; (3) the uncertainty in the remote stress field is not accounted for; (4) unmapped faults are missing; and (5) the presence of the salt layer on top of the reservoir is not properly handled. Some of these issues have been already tested. As an example, switching from our base case scenario (where the fault pressure follows the pressure of the most depleted compartment) to the scenario where we take fault pressure equal to the average pressure of the two compartments did not lower the residuals. Because of computational constraints, the detailed modeling of the flow inside the faults and at their boundaries, which will require a local mesh refinement, is currently unachievable. Thus, one cannot exclude that local gradients of pore pressure, currently missing in our approach, could drive additional stress changes (see Chang & Segall, 2016a, 2016b; Rutqvist et al., 2016) and explain the persistent mismatch with observations. Selecting a slightly different remote stress tensor did not help to reconcile the observed and modeled event density spatial pattern. The top seal Zechstein salt layer probably plays a role in both (i) the stress distribution on top of the reservoir and (ii) the effective frictional behavior of the Groningen faults. Still at the level of the induced stress computation, we made the assumption of a uniform distribution of elastic properties of the reservoir and underburden. In doing so, we are missing the spatial heterogeneities in the compaction coefficient, which certainly affect the compaction field as pointed out by linear inversion of subsidence measurements (Bierman et al., 2015; Fokker & Van Thienen-Visser, 2016). This last effect might be, at least partially, at the origin of the residual pattern observed for both subareas.

We have shown that since the production onset in the two subareas of interest, the characteristic periods of stress perturbations T (caused by production rate fluctuations) are much shorter than the characteristic response time T_a of the Groningen fault system. In this regime $T \ll T_a$ the variations of the seismicity rate are in phase with the Coulomb stress change and present a delay with respect to the Coulomb stress rate of a quarter of the perturbation period T. However, one important feature of the Groningen fault system in the two subareas of interest is that its seismicity is unsteady since the start of production and T_a has been shortening due to the induced increase of the background stressing rate. Since the Groningen faults are probably not yet at steady state in the two selected subareas, the shortening of t_a is continuing, and our approach predicts the Groningen system to become gradually more responsive to the stressing rate.

Applying Dieterich's seismicity rate modeling under the assumption of steady state at the beginning of the analysis period provides only apparent background stressing and seismicity rates. It results that such apparent background stressing and seismicity rates have been constantly increasing since the start of production, but the fault constitutive parameter A remained constant. Our modeling approach gives access to the parameters values in 1993 and reveals significant contrasts between the C-area and SW-area. Notably, $t_a(1993)$ is much longer for the SW-area compared to the C-area, which could explain the late ramp-up of the seismicity for the SW-area. Spatial heterogeneities in the rate-and-state parameters can thus account, at least partially, for differences in the seismicity patterns between the two subareas. This last result would not be captured by studying the entire Groningen field as a whole as pursued in previous attempts (Bourne et al., 2014; Bourne et al., 2018; Bourne & Oates, 2017; Dempsey & Suckale, 2017), which would only provide an averaged or smoothed version of the dynamics. Another factor contributing to the contrasted seismicity pattern between the two subareas is the difference in induced stressing rate history. Clearly, the spatial heterogeneities of both the induced stressing rate history and rate-and-state parameters have to be considered in the modeling of the induced seismicity at the Groningen field.

The relative delay in the seismicity response at the onset of reservoir depletion, despite a significant stress increase (Candela et al., 2018; van Wees et al., 2014), has been interpreted as resulting from the fact that the stress on the Groningen faults was far from criticality at the onset of depletion (Bourne & Oates, 2017; Candela et al., 2018; Dempsey & Suckale, 2017; Muntendam-Bos & de Waal, 2013; van Wees et al., 2014). A different explanation is offered by Dieterich's theory, where at the onset of depletion, the seismicity rate is assumed steady state and the Groningen faults are assumed to be already close to criticality. Faults in Dieterich's model are thus always active, generating events, although at a very low rate if the loading rate is very low, as in Groningen. We deduced from our modeling approach a low background seismicity rate in 1993. Also, we expect an even lower value at the start of production when the system was at steady state, which is expected for an intraplate region such as the North of the Netherlands. Because of this very low background seismicity rate, changes in stressing rate due to the onset of reservoir depletion, even at a fast production rate, may not be sufficiently large to induce a noticeable change in seismicity rate. It is only after the seismicity rate ramped up to a noticeable rate around 1990 that the changes were identified.

Appendix A

A1. Upscaling of the Stress Rate

Following the approach described in section 3.1, we can calculate the effective normal stress and shear stress and their respective rates for every observation point along each fault (Figure 2). Observation points are placed on fault pillars, which in turn make up the 3-D geometry of a fault (Figure 2). When considering the entire Groningen field, the model contains over two million observation points, distributed over about 21,000 pillars on a total of more than 800 faults. Upscaling of the stress results is desirable because in order to compare a particular model realization with the observed seismicity, the dimensionality of the model output and the data needs to be the same.

There are a number of ways in which the upscaling from three spatial dimensions to two spatial dimensions can be achieved. We describe two routes here.

The first approach consists in calculating first the seismicity rate using Dieterich's approach at each observation point and then calculating the integral over each pillar to get the seismicity rate per pillar in 2-D. This approach is strictly the “correct approach.” It is however not practically suitable for the data assimilation step since computing an ensemble of realizations following this procedure would take very long on a typical desktop computer.

The second approach consists of upscaling first the stress components (effective normal stress, shear stress, and their respective rates). We calculate first the Coulomb stressing rate $\dot{S}$ for each observation point, and we select the location of the maximum value for each pillar. Then, in order to upscale all the stress components, for each pillar we pick their respective values at the selected location of the maximum $\dot{S}$. We can now compute the seismicity rate for each pillar following Dieterich's theory (equation (4)). This approach offers the advantage to be computationally very fast and suitable for exploring a large number of realizations during the conditioning step. The downside of this approach is that stress peaks at the reservoir edges can control the maximum $\dot{S}$. However, it is not possible to relax these stress peaks which are intrinsic to our elasticity assumption. Even for the correct approach, these stress peaks are part of the integral. Still, it is important to note here that our approximation captures the temporal dynamic of the seismicity rate at each pillar location (see Figure A1). This can be explained by the fact that for each pillar the integrated seismicity rate for all the observation points is expected to be dominated by the location where the seismicity rate is the highest (Kroll et al., 2017). The relative seismicity rate R predicted by this upscaling approach is overall higher

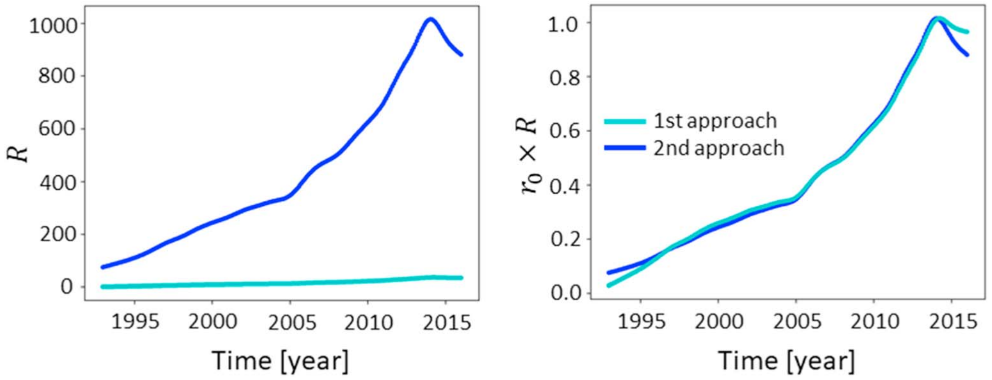

Figure A1. (left) Time series of the relative seismicity rate R along one arbitrary observation point. (right) After scaling with r_0, the two upscaling approaches show similar temporal patterns.

than for the correct approach described above, even if the temporal dynamic is identical for both approaches. Adjusting r_0 for calculating the seismicity rate R_D (see equation (3)) resolves this offset.

A2. Response of an Unsteady Fault System to Harmonic Stress Perturbations

Ader et al. (2014) have derived the rate-and-state seismicity response to harmonic stress perturbations of a fault population relative to a steady state. We address here the same problem but when the reference state of the fault population is unsteady, which is the relevant scenario for the Groningen fault system.

We assume that the loading is composed of a long-term, unsteady loading $\dot{S}_u(t)$ and a short-term perturbation $\dot{s}(t)$

$$\dot{S} = \dot{S}_u + \dot{s} \tag{A1}$$

In our Groningen case study, the long-term unsteady loading corresponds to the 10-year long-period fluctuations of the stressing rate, and the short-term perturbation corresponds to the 1-year short-period fluctuations of the stressing rate. We define the reference state $\gamma_0(t)$ as the unsteady state resulting from $\dot{S}_u(t)$, that is, the time-dependent solution to Dieterich's equation (equation (2)) with $\dot{S} = \dot{S}_u(t)$

$$a\sigma\dot{\gamma}_0 = 1 - \gamma_0\dot{S}_u \tag{A2}$$

We define a perturbation $\delta\gamma(t)$ relative to the reference state by $\gamma = \gamma_0 + \delta\gamma$. We assume that the perturbation is small, $\frac{\delta\dot{\gamma}}{\dot{\gamma}_0} \ll 1$ and $\frac{\delta\gamma}{\gamma_0} \ll 1$ and expand Dieterich's equation to first order

$$a\sigma\,\delta\dot{\gamma} = -\delta\gamma\dot{S}_u - \gamma_0\dot{s} \tag{A3}$$

We assume that the fluctuations of the reference loading are much slower than those of the loading perturbation. Taking the short-time Fourier transform of the previous equation over a time window much shorter than the characteristic time scales of $\dot{S}_u(t)$, we obtain

$$\frac{\delta\gamma(\omega)}{\gamma_0} = -\frac{\dot{s}(\omega)/\dot{S}_u}{1 + i\omega\frac{a\sigma}{\dot{S}_u}} \tag{A4}$$

In terms of the perturbation $\delta R(t)$ of the seismicity rate $R(t)$ relative to the reference rate $R_0(t)$,

$$\frac{\delta R(\omega)}{R_0(t)} = \frac{\dot{s}(\omega)/\dot{S}_u(t)}{1 + i\omega\frac{a\sigma}{\dot{S}_u(t)}} \tag{A5}$$

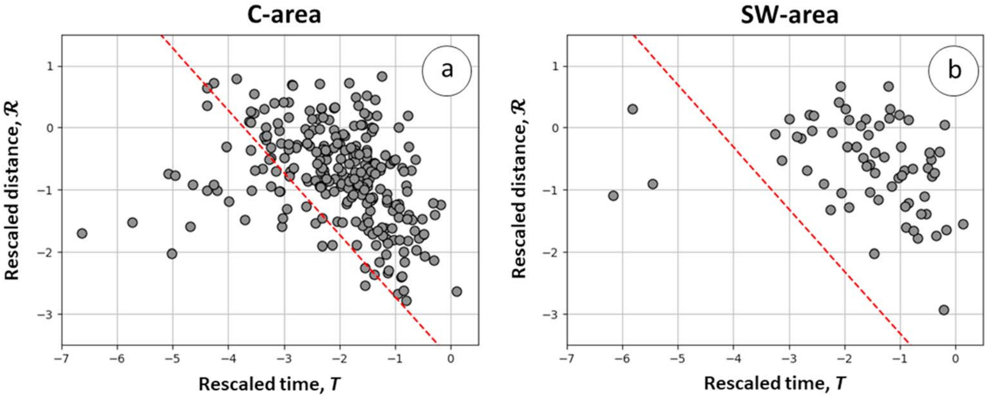

Figure A2. Bimodal distribution of time and space components ($\log_{10}T$, $\log_{10}\mathscr{R}$) of the nearest-neighbor distance η for the C-area (a) and SW-area (b) over the period (1993–2016) and with a minimum magnitude of 1.0. Each gray circle in these plots corresponds to a catalogue event; its location in the ($log_{10}T$, $\log_{10}\mathscr{R}$) plane provides information about the time and space distance to the event's parent. The threshold value $\log_{10}\eta_0$ to separate the two modes is estimated used a 1-D Gaussian mixture model applied to the logarithmic nearest-neighbor distances $\log_{10}\eta_{ij}$ (Hicks, 2011). The red dashed diagonal lines depict the $\log_{10}\eta_0$. On the right of the red dashed diagonal lines, these are the independent mainshocks and on the left the clustered aftershocks.

This is similar to equation B5 of Ader et al. (2014), but the characteristic time scale controlling the spectrum of the sensitivity to stress perturbations is now

$$t_a(t) = \frac{a\sigma}{\dot{S}_u(t)} \tag{A6}$$

In particular, the effective $t_a(t)$ is now time dependent; it changes with the evolving long-term loading.

A3. Declustering

We employed the statistical methodology for clustering analysis of seismicity initially introduced in Zaliapin et al. (2008). Only the main ingredients of the approach are given here, and we encourage the reader to dig for more details in Zaliapin et al. (2008), Zaliapin and Ben-Zion (2013), and Zaliapin and Ben-Zion (2016).

The declustering algorithm of Zaliapin et al. (2008) is based on space-time-magnitude distances between earthquakes i and j defined by Baiesi and Paczuski (2004) as

$$\eta_{ij} = \begin{cases} t_{ij}\left(r_{ij}\right)^{d}10^{-bm_i}, & t_{ij}>0 \\ \infty, & t_{ij}\leq 0 \end{cases} \tag{A7}$$

t_{ij} is the event intercurrence time in years, which is positive if event j occurred after event i ($t_{ij} = t_j - t_i$), $r_{ij} \geq 0$ is the spatial distance between the earthquake hypocenters in kilometers, m_i is the magnitude of event i, d is the (possibly fractal) dimension of the hypocenters, and b corresponds to the b-value of the Gutenberg-Richter frequency-magnitude distribution.

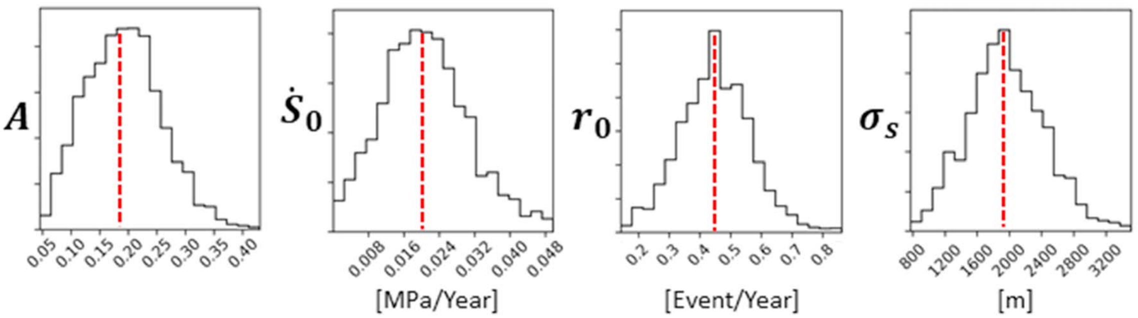

Figure A3. Marginal probability distributions obtained with the Markov Chain Monte Carlo search (with a minimum magnitude of 1.0) confronting the model with the declustered catalogue for the C-area and for the training period (1993–2016). Bounded uniform prior distributions for each model parameters are A: $\mathbf{U}(1e^{-3}, 10)$, $\dot{S}_0$: $\mathbf{U}(5e^{-6}, 0.5)$, r_0: $\mathbf{U}(5e^{-4}, 5)$, σ_s: $\mathbf{U}(500, 4{,}500)$—with $\mathbf{U}$(a, b) is a uniform distribution between a and b.

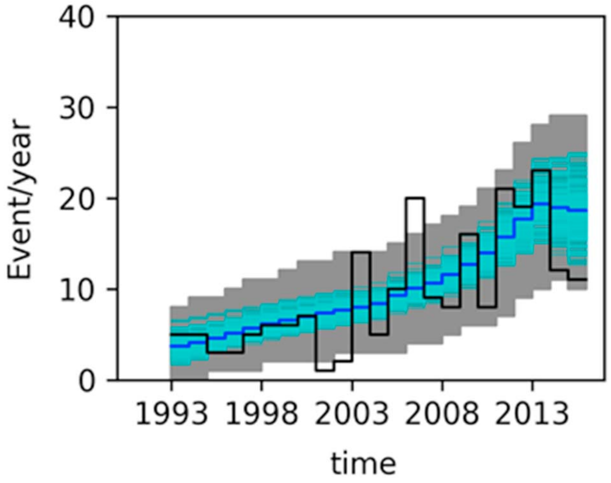

Figure A4. Predicted seismicity history (annual event rate) for the C-area after calibration during the training period (1993–2016) with the declustered catalogue (and minimum magnitude = 1.0). The model corresponds to 300 realizations (cyan) randomly drawn from the posterior density distribution. The mean of the models is displayed in blue. The gray region indicates 95% of the distribution when stochastic Poisson variabilities are accounted for. For each posterior member, 30 synthetic catalogues are generated in order to account for stochastic Poisson variabilities. The gray region indicates 95% of the distribution of the 9,000 synthetic catalogues.

The nearest-neighbor distance for a given event j is the minimum distance among η_{ij} where i goes over all earlier events in the catalogue. The event i that corresponds to the nearest-neighbor distance is called the nearest-neighbor, or parent, of event j.

Zaliapin et al. (2008) proposed to consider the scalar distance η in terms of its space and time components normalized by the magnitude of the parent event i as

$$T_{ij} = t_{ij}10^{-qbm_i}; \quad \mathcal{R}_{ij} = \left(r_{ij}\right)^{d}10^{-pbm_i}; \qquad p+q=1 \tag{A8}$$

And now

$$\log_{10}\eta_{ij} = \log_{10}T_{ij} + \log_{10}\mathcal{R}_{ij} \tag{A9}$$

For our analysis, we fix $b = 1$, $d = 1.6$, and $p = 0.5$ as followed by Zaliapin and Ben-Zion (2016). Zaliapin and Ben-Zion (2013) have demonstrated that the estimated cluster structure is stable with respect to the parameter values; our conclusions are thus expected to be nonsensitive to the precise parameter values.

Zaliapin et al. (2008) and Zaliapin and Ben-Zion (2016) have shown that observed seismicity generally presents a bimodal joint distribution of $(\log_{10}T, \log_{10}\mathcal{R})$. In our case, one mode corresponds to the independent mainshocks, whereas the other consists of clustered aftershock events located considerably closer in time and space to their parents. Figure A2 shows the 2-D joint distributions of the rescaled time and space component $(T, \mathcal{R})$ of the nearest-neighbor earthquake distance η for the C-area and SW-area. For the SW-area, over a total of 67 events, only three events are identified as clustered aftershock events. For the C-area, 39 clustered aftershock events are identified and 219 mainshocks that is approximately 18% of aftershocks.

The C-area model parameters can now be reestimated with the declustered catalogue. Their posterior distributions (Figure A3) are almost identical to the ones obtained with the original catalogue including aftershock events (see Figure 5). For the sake of completeness in our analysis, Figure A4 displays the ensemble of posterior event rate predictions for the C-area with model parameters obtained with the declustered catalogue. As observed in Figure 6a with the original catalogue, this ensemble of posterior predictions matches the low-frequency temporal fluctuations of the declustered catalogue.

Acknowledgments
This study benefits from lengthily discussions with TNO's colleagues about the peculiar aspects of the Groningen induced seismicity. We thank here especially Jaap Breunese, Dirk Kraaijpoel, Joana Esteves Martins, Karin Thienen-Visser, Ingrid Kroon, Joost Roholl, Manuel Nepveu, Loes Buijze, Jan ter Heege, and Orlic Bogdan. The first author also thanks Emily Brodsky for insightful conversations at various stages of this study. Finally, we also gratefully acknowledge two anonymous reviewers whose suggestions greatly improved our initial contribution. The 4-D yearly induced stress changes and pore pressures at faults and the earthquake catalogue are available as supporting information and in an open access data repository (Candela & Pluymaekers, 2019). The earthquake catalogue was obtained from KNMI at their website (www.knmi.nl).

References

Ader, T., Lapusta, N., Avouac, J.-P., & Ampuero, J. P. (2014). Response of rate-and-state seismogenic faults to harmonic shear-stress perturbations. *Geophysical Journal International*, *198*(1), 385–413. https://doi.org/10.1093/gji/ggu144

Baiesi, M., & Paczuski, M. (2004). Scale-free networks of earthquakes and aftershocks. *Physical Review E*, *69*(6), 066106. https://doi.org/10.1103/PhysRevE.69.066106

Barnes, J., & Hut, P. (1986). A hierarchical O(N log N) force-calculation algorithm. *Nature*, *324*(6096), 446–449. https://doi.org/10.1038/324446a0

Beeler, N. M., & Lockner, D. A. (2003). Why earthquakes correlate weakly with the solid Earth tides: Effects of periodic stress on the rate and probability of earthquake occurrence. *Journal of Geophysical Research*, *108*(B8), 2391. https://doi.org/10.1029/2001JB001518

Bierman, S., Kraaijeveld, F., & Bourne, S. (2015). Regularised direct inversion to compaction in the Groningen reservoir using measurements from optical leveling campaigns. Technical Report. Shell Global Solutions International. Amsterdam.

Bourne, S. J., & Oates, S. J. (2017). Extreme threshold failures within a heterogeneous elastic thin-sheet and the spatial-temporal development of induced seismicity within the Groningen gas field. *Journal of Geophysical Research: Solid Earth*, *122*, 10,299–10,320. https://doi.org/10.1002/2017JB014356

Bourne, S. J., Oates, S. J., & van Elk, J. (2018). The exponential rise of induced seismicity with increasing stress levels in the Groningen gas field and its implications for controlling seismic risk. *Geophysical Journal International*, *213*, 1693–1700.

Bourne, S. J., Oates, S. J., van Elk, J., & Doornhof, D. (2014). A seismological model for earthquakes induced by fluid extraction from a subsurface reservoir. *Journal of Geophysical Research: Solid Earth*, *119*, 8991–9015. https://doi.org/10.1002/2014JB011663

Buijze, L., van den Bogert, P. A. J., Wassing, B. B. T., Orlic, B., & ten Veen, J. (2017). Fault reactivation mechanisms and dynamic rupture modelling of depletion-induced seismic events in a Rotliegend gas reservoir. *Netherlands Journal of Geosciences - Geologie en Mijnbouw*, *96*(5), s131–s148.

Candela, T. and Pluymaekers, M. (2019). Dataset for "Depletion-induced seismicity at the Groningen gas field: Coulomb rate-and-state models including differential compaction effect" [dataset]. Zenodo. https://doi.org/10.5281/zenodo.2530753

Candela, T., Wassing, B., ter Heege, J., & Buijze, L. (2018). How earthquakes are induced. *Science*, *360*(6389), 598–600. https://doi.org/10.1126/science.aat2776

Catalli, F., Cocco, M., Console, R., & Chiaraluce, L. (2008). Modeling seismicity rate changes during the 1997 Umbria-Marche sequence (central Italy) through rate- and state-dependent model. *Journal of Geophysical Research*, *113*, B11301. https://doi.org/10.1029/2007JB005356

Cattania, C., Hainzl, S., Wang, L., Enescu, B., & Roth, F. (2015). Aftershock triggering by postseismic stresses: A study based on Coulomb rate-and-state models. *Journal of Geophysical Research: Solid Earth*, *120*, 2388–2407. https://doi.org/10.1002/2014JB011500

Chang, K. W., & Segall, P. (2016a). Injection induced seismicity on basement faults including poroelastic stressing. *Journal of Geophysical Research: Solid Earth*, *121*, 2708–2726. https://doi.org/10.1002/2015JB012561

Chang, K. W., & Segall, P. (2016b). Seismicity on Basement Faults Induced by Simultaneous Fluid Injection–Extraction. *Pure and Applied Geophysics*, *173*(8), 2621–2636. https://doi.org/10.1007/s00024-016-1319-7

Chen, J., & Spiers, C. J. (2016). Rate and state frictional and healing behavior of carbonate fault gouge explained using microphysical model. *Journal of Geophysical Research: Solid Earth*, *121*, 8642–8665. https://doi.org/10.1002/2016JB013470

Daniel, G., Fortier, E., Romijn, R., & Oates, S. (2016). *Location results from borehole microseismic monitoring in the Groningen gas reservoir, Netherlands, in 6th EAGE Workshop on Passive Seismic* (pp. 87–93). Muscat, Oman: EAGE.

Dempsey, D., & Suckale, J. (2017). Physics-based forecasting of induced seismicity at Groningen gas field, the Netherlands. *Geophysical Research Letters*, *44*, 7773–7782. https://doi.org/10.1002/2017GL073878

de Waal, A., Muntendam-Bos, A. G., & Roest, J. P. A. (2015). Production induced subsidence and seismicity in the Groningen gas field—Can it be managed? *Proceedings of the International Association of Hydrological Sciences*, *372*, 129–139. https://doi.org/10.5194/piahs-372-129-2015

Dieterich, J. H. (1994). A constitutive law for rate of earthquake production and its application to earthquake clustering. *Journal of Geophysical Research*, *99*(B2), 2601–2618. https://doi.org/10.1029/93JB02581

Dieterich, J. H., Cayol, V., & Okubu, P. (2000). The use of earthquake rate changes as a stress meter at Kilauea volcano. *Nature*, *40*.

Dieterich, J. H., & Kilgore, B. (1996). Implications of fault constitutive properties for earthquake prediction. *Proceedings of the National Academy of Sciences of the United States of America*, *93*(9), 3787–3794. https://doi.org/10.1073/pnas.93.9.3787

Dost, B., Goutbeek, F., van Eck, T., & Kraaijpoel, D. (2012). Monitoring induced seismicity in the North of the Netherlands: Status report 2010. Royal Netherlands Meteorological Institute, Scientific report WR 2012-03: 1–39.

Dost, B., & Kraaijpoel, D. (2013). The August 16, 2012 earthquake near Huizinge (Groningen). Tech. Rep. January, KNMI, de Bilt, The Netherlands.

Dost, B., Ruigrok, E., & Spetzler, J. (2017). Development of seismicity and probabilistic hazard assessment for the Groningen gas field. *Netherlands Journal of Geosciences - Geologie en Mijnbouw*, *96*(5).

Fokker, P. A., & Van Thienen-Visser, K. (2016). Inversion of double-difference measurements from optical leveling for the Groningen gas field. *International Journal of Applied Earth Observation and Geoinformation*, *49*, 1–9. https://doi.org/10.1016/j.jag.2016.01.004

Foreman-Mackey, D., Hogg, D. W., Lang, D., & Goodman, J. (2013). emcee: The MCMC hammer. *Publications of the Astronomical Society of the Pacific*, *125*(925), 306–312. https://doi.org/10.1086/670067

Geertsma, J. (1973). A basic theory of subsidence due to reservoir compaction: The homogeneous case. *Verh Kon Ned Geol Mijnbouwkundig Genootschap*, *28*, 43–62.

Hainzl, S., Enescu, B., Cocco, M., Woessner, J., Catalli, F., Wang, R., & Roth, F. (2009). Aftershock modeling based on uncertain stress calculations. *Journal of Geophysical Research*, *114*, B05309. https://doi.org/10.1029/2008JB006011

Heimisson, E. R. (2019). Constitutive law for earthquake production based on rate-and-state friction: Theory and application of interacting sources. *Journal of Geophysical Research: Solid Earth*, *124*, 1802–1821. https://doi.org/10.1029/2018JB016823

Heimisson, E. R., & Segall, P. (2018). Constitutive law for earthquake production based on rate-and-state friction: Dieterich 1994 revisited. *Journal of Geophysical Research: Solid Earth*, *123*, 4141–4156. https://doi.org/10.1029/2018JB015656

Hettema, M. H., Jaarsma, B., Schroot, B. M., & van Yperen, G. C. N. (2017). An empirical relationship for the seismic activity rate of the Groningen gas field. *Netherlands Journal of Geosciences - Geologie en Mijnbouw*, *96*(5), s149–s161.

Hicks, A. (2011). Clustering in multidimensional spaces with applications to statistical analysis of earthquake clustering, MSc Thesis, Department of Mathematics and Statistics, University of Nevada, Reno.

Hunfeld, L. B., Niemeijer, A. R., & Spiers, C. J. (2017). Frictional properties of Simulated fault gouges from the seismogenic Groningen Gas field under in situ P-T-chemical conditions. *Journal of Geophysical Research: Solid Earth*, *122*, 8969–8989. https://doi.org/10.1002/2017JB014876

Inbal, A., Ampuero, J. P., & Avouac, J. P. (2017). Locally and remotely triggered aseismic slip on the central San Jacinto Fault near Anza, CA, from joint inversion of strain and earthquake data. *Journal of Geophysical Research: Solid Earth*, *122*, 3033–3061. https://doi.org/10.1002/2016JB013499

Jagt, L., Ruigrok, E., & Paulssen, H. (2017). Relocation of clustered earthquakes in the Groningen gas field. *Netherlands Journal of Geosciences - Geologie en Mijnbouw*, *96*(5).

Kroll, K. A., Richards-Dinger, K. B., Dieterich, J. H., & Cochran, E. S. (2017). Delayed seismicity rate changes controlled by static stress transfer. *Journal of Geophysical Research: Solid Earth*, *122*, 7951–7965. https://doi.org/10.1002/2017JB014227

Llenos, A. L., & McGuire, J. J. (2011). Detecting aseismic strain transients from seismicity data. *Journal of Geophysical Research*, *116*, B06305. https://doi.org/10.1029/2010JB007537

Llenos, A. L., McGuire, J. J., & Ogata, Y. (2009). Modeling seismic swarms triggered by aseismic transients. *Earth and Planetary Science Letters*, *281*(1-2), 59–69. https://doi.org/10.1016/j.epsl.2009.02.011

Llenos, A. L., & Michael, A. J. (2013). Modeling earthquake rate changes in Oklahoma and Arkansas: Possible signatures of induced seismicity. *Bulletin of the Seismological Society of America*, *103*(5), 2850–2861. https://doi.org/10.1785/0120130017

Lockner, D. A., & Beeler, N. M. (1999). Premonitory slip and tidal triggering of earthquakes. *Journal of Geophysical Research*, *104*(B9), 20,133–20,151. https://doi.org/10.1029/1999JB900205

Marone, C. (1998). Laboratory-derived friction laws and their application to seismic faulting. *Annual Review of Earth and Planetary Sciences*, *26*(1), 643–696. https://doi.org/10.1146/annurev.earth.26.1.643

Mindlin, R. D. (1936). Force at a point in the interior of a semi-infinite solid. *Physics*, *7*(5), 195–202. https://doi.org/10.1063/1.1745385

Nederlandse Aardolie Maatschappij (NAM) (2016). Technical addendum to the Winningsplan Groningen 2016; Production, subsidence, induced earthquakes and Seismic hazard and risk assessment in the Groningen field (57 pp.). Retrieved from http://www.nam.nl/algemeen/mediatheek-en-downloads/winningsplan-2016.html

Nederlandse Aardolie Maatschappij (NAM) (2017). Groningen dynamic model update 2017. Retrieved from https://nam-onderzoeksrapporten.data-app.nl/reports/download/groningen/en/d67cb8ac-e5b0-4130-9598-5b7fc83edae2

Mulders, F. M. M. (2003). Modelling of stress development and fault slip in and around a producing gas reservoir, PhD thesis, Technical University of Delft.

Muntendam-Bos, A. G., & de Waal, J. A. (2013). Reassessment of the probability of higher magnitude earthquakes in the Groningen gas field. SodM technical report.

Muntendam-Bos, A. G., Roest, J. P. A., & de Waal, J. A. (2017). The effect of imposed production measures on gas extraction induced seismic risk. *Netherlands Journal of Geosciences - Geologie en Mijnbouw*, *96*(5), s271–s278.

Nepveu, M., van Thienen-Visser, K., & Sijacic, D. (2016). Statistics of seismic events at the Groningen field. *Bulletin of Earthquake Engineering*, *14*(12), 3343–3362. https://doi.org/10.1007/s10518-016-0007-4

Niemeijer, A. R., & Spiers, C. J. (2007). A microphysical model for strong velocity weakening in phyllosilicate-bearing fault gouges. *Journal of Geophysical Research*, *112*, B10405. https://doi.org/10.1029/2007JB005008

Ogata, Y. (1998). Space-time point-process models for earthquake occurrences. *Annals of the Institute of Statistical Mathematics*, *50*(2), 379–402. https://doi.org/10.1023/A:1003403601725

Ogata, Y. (2011). Significant improvements of the space-time ETAS model for forecasting of accurate baseline seismicity. *Earth Planets Space*, *63*(3), 217–229. https://doi.org/10.5047/eps.2010.09.001

Okada, Y. (1992). Internal deformation due to shear and tensile faults in a half-space. *Bulletin of the Seismological Society of America*, *82*(2), 1018–1040.

Orlic, B., & Wassing, B. B. T. (2013). A study of stress change and fault slip in producing gas reservoirs overlain by elastic and viscoelastic caprocks. *Rock Mechanics and Rock Engineering*, *46*(3), 421–435. https://doi.org/10.1007/s00603-012-0347-6

Rhoades, D. A., Schorlemmer, D., Gerstenberger, M. C., Christophersen, A., & Zechar, D. (2011). M., Imoto (2011). Efficient testing of earthquake forecasting models. *Acta Geophysica*, *59*(4), 728–747. https://doi.org/10.2478/s11600-011-0013-5

Roest, J. P. A., & Kuilman, W. (1994). Geomechanical analysis of small earthquakes at the Eleveld gas reservoir. Eurock'94. Balkema, A.A. (Rotterdam): 573–580. Conference proceedings.

Rubin, A. M., & Ampuero, J. P. (2007). Aftershock asymmetry on a bimaterial interface. *Journal of Geophysical Research*, *112*, B05307. https://doi.org/10.1029/2006JB004337

Rutqvist, J., Rinaldi, A. P., Cappa, F., Jeanne, P., Mazzoldi, A., Urpi, L., et al. (2016). Fault activation and induced seismicity in geological carbon storage—Lessons learned from recent modeling studies. *Journal of Rock Mechanics and Geotechnical Engineering*, *8*(6), 789–804. https://doi.org/10.1016/j.jrmge.2016.09.001

Schorlemmer, D., Gerstenberger, M. C., Wiemer, S., Jackson, D. D., & Rhoades, D. A. (2007). Earthquake likelihood model testing. *Seismological Research Letters*, *78*(1), 17–29. https://doi.org/10.1785/gssrl.78.1.17

Segall, P., & Fitzgerald, S. D. (1998). A note on induced stress changes in hydrocarbon and geothermal reservoirs. *Tectonophysics*, *289*(1-3), 117–128. https://doi.org/10.1016/S0040-1951(97)00311-9

Segall, P., & Lu, S. (2015). Injection-induced seismicity: Poroelastic and earthquake nucleation effects. *Journal of Geophysical Research: Solid Earth*, *120*, 5082–5103. https://doi.org/10.1002/2015JB012060

Sijacic, D., Pijpers, F., Nepveu, M., & van Thienen-Visser, K. (2017). Statistical evidence on the effect of production changes on induced seismicity. *Netherlands Journal of Geosciences - Geologie en Mijnbouw*, *96*(5).

Toda, S., Stein, R. S., & Sagiya, T. (2002). Evidence from the AD 2000 Izu islands earthquake swarm that stressing rate governs seismicity. *Nature*, *419*(6902), 58–61.

Van den Bogert, P. A. J. (2015). Impact of various modelling options on the onset of fault slip and fault slip response using 2-dimensional finite-element modelling. Restricted, Report No. SR.15.11455. Shell Global Solutions International B.V. (Rijswijk).

Van Geuns, L., & Thienen-Visser, K. (2017). Editorial-special issue Netherlands Journal of Geosciences on Induced seismicity in the Groningen gas field. *Netherlands Journal of Geosciences*, *96*.

van Wees, J. D., Buijze, L., Van Thienen-Visser, K., Nepveu, M., Wassing, B. B. T., Orlic, B., & Fokker, P. A. (2014). Geomechanics response and induced seismicity during gas field depletion in the Netherlands. *Geothermics*, *52*, 206–219. https://doi.org/10.1016/j.geothermics.2014.05.004

van Wees, J. D., Fokker, P. A., Van Thienen-Visser, K., Wassing, B. B. T., Osinga, S., Orlic, B., et al. (2017). Geomechanical models for induced seismicity in the Netherlands: Inferences from simplified analytical, finite element and rupture model approaches. *Netherlands Journal of Geosciences*, *96*(5), s183–s202. https://doi.org/10.1017/njg.2017.38

van Wees, J. D., Osinga, S., Van Thienen-Visser, K., & Fokker, P. A. (2018). Reservoir creep and induced seismicity: Inferences from geomechanical modeling of gas depletion in the Groningen field. *Geophysical Journal International*, *212*(3), 1487–1497. https://doi.org/10.1093/gji/ggx452

Willacy, C., van Dedem, E., Minisini, S., Li, J., Blokland, J. W., Das, I., & Droujinine, A. (2018). Application of full-waveform event location and moment-tensor inversion for Groningen induced seismicity, *The Leading Edge*, *37*(2), 92–99. https://doi.org/10.1190/tle37020092.1

Zaliapin, I., & Ben-Zion, Y. (2013). Earthquake clusters in southern California, I: Identification and stability. *Journal of Geophysical Research: Solid Earth*, *118*, 2847–2864. https://doi.org/10.1002/jgrb.50179

Zaliapin, I., & Ben-Zion, Y. (2016). Discriminating characteristics of tectonic and human-induced seismicity. *Bulletin of the Seismological Society of America*, *106*(3), 846–859. https://doi.org/10.1785/0120150211

Zaliapin, I., Gabrielov, A., Keilis-Borok, V., & Wong, H. (2008). Clustering analysis of seismicity and aftershock identification. *Physical Review Letters*, *101*(1), 018501. https://doi.org/10.1103/PhysRevLett.101.018501

Zechar, D., Gerstenberger, M. C., & Rhoades, D. A. (2010). Likelihood-based tests for evaluating space-rate-magnitude earthquake forecasts. *Bulletin of the Seismological Society of America*, *100*(3), 1184–1195. https://doi.org/10.1785/0120090192

Zhuang, J., Harte, D., Werner, M. J., Hainzl, S., & Zhou, S. (2012). Basic models of seismicity: Temporal models, Community Online Resource for Statistical Seismicity Analysis. https://doi.org/10.5078/corssa-79905851

Zhuang, J., & Touati, S. (2015). Stochastic simulation of earthquake catalogs, Community Online Resource for Statistical Seismicity Analysis. https://doi.org/10.5078/corssa-43806322, http://www.corssa.org

Ziv, A., & Rubin, A. M. (2003). Implications of rate-and-state friction for properties of aftershock sequences: Quasi-static inherently discrete simulations. *Journal of Geophysical Research*, *108*, 2051. https://doi.org/10.1029/2001JB001219